Version of Record: https://www.sciencedirect.com/science/article/pii/S0022460X23005801
Manuscript_067fca6bad8e3620d11a9a2dfe054ddc

Exploring effective TET through a vibro-impact nonlinear energy sink over broad parameter regimes

Rahul Kumar[a], Rachel Kuske[a,*], Daniil Yurchenko[b]

[a]*School of Mathematics, Georgia Institute of Technology, Atlanta, USA.*
[b]*Institute of Sound and Vibration Research, University of Southampton, UK.*

Abstract

In recent times, the vibro-impact nonlinear energy sink (VINES) has emerged as a promising passive mechanism for vibration mitigation in engineering systems. The VINES system consists of a ball travelling within a cavity of an externally excited linear oscillator (LO). The ball impacts either end of the cavity, transferring energy from the LO to the ball and mitigating excess oscillations of the LO. Earlier studies of VINES analysed scenarios with the mass of the ball to be small relative to the LO, with low forcing amplitude near the resonant frequency of the LO. Improvements in targeted energy transfer (TET), observed for an increased mass of the ball, motivate an investigation of VINES for larger mass ratios, using a recently developed semi-analytical map-based approach that provides the exact solution without the limitations of previous analyses. Complementary analytical and numerical approaches treat larger mass ratios and higher amplitudes of the external harmonic excitation for forcing frequencies away from the natural frequency of the LO, identifying parameter regimes for efficient and inefficient performance based on standard measures of energy transfer. The analysis identifies multiple regions for the desired behavior with two alternating impacts per forcing period and provides relevant stability conditions. Numerical results indicate chattering behavior in regimes where energy transfer is minimal, yielding performance that appears similar to resonance. This phenomenon can be directly related to the passive nature of the VINES design, where the natural frequency of the VINES system decreases as the mass of the ball, and thus that of the system, increases. Then the peak response of the LO is shifted away from its resonant frequency, allowing excellent energy transfer to be realized there.

Keywords: non-smooth system, targeted energy transfer, vibro-impact system, bifurcation analysis, VINES

*Corresponding author.
Email addresses: rahul.kumar@math.gatech.edu (Rahul Kumar), rachel@math.gatech.edu (Rachel Kuske), d.yurchenko@soton.ac.uk (Daniil Yurchenko)

1. Introduction

For vibrating engineering structures, the quest for effective vibration control strategies remains a perpetual challenge, vital for ensuring the longevity and efficiency of machinery and structures. To mitigate these excessive vibrations, passive vibration control mechanisms are preferred, particularly when safeguarding delicate structures and sensitive machinery. Among these strategies, Targeted Energy Transfer (TET) is one such passive mechanism of vibration attenuation for forced engineering systems. The core concept of TET revolves around the attachment of a secondary structure to the primary one, strategically employed to curtail the primary structure's oscillations. Notably, the energy transferred from the primary structure to the secondary system is irreversible and can be dissipated through dampers or used for scavenging the electrical energy [1–4]. In a conventional TET approach, a second spring mass system is attached and tuned to a primary linear spring mass system. The effectiveness of this arrangement near the natural frequency of the primary system and the limitation of the magnitude of the secondary mass have proved to be a bottleneck in its widespread application [5]. To broaden the frequency range for effective TET, a nonlinear energy transfer mechanism is developed, attaching the primary structure with a nonlinear energy sink (NES), is developed. Traditionally, it is realized through a model employing a nonlinear spring and a linear damper to connect the secondary system to the primary structure [6, 7]. However, this approach demands meticulous tuning with the primary structure to optimize TET's performance across specific frequency ranges [8]. It has also been shown that for a freely vibrating system, TET will be realized only when the input energy to the system reaches the threshold value that could engage the NES [8, 9].

There are various types of NES based on the implementation of nonlinearity in the model, such as NES with piecewise nonlinearity [10], NES with nonlinear dampers [11] or vibro-impact nonlinear energy sink (VINES) [12, 13]. Among the various NES models, recent studies report VINES as one of the promising approaches for TET, where energy is dissipated through impacts when the coefficient of restitution is less than unity. Also, energy transfer through VINES happens on a relatively fast time scale and is a desirable feature for the rapid control of vibration amplitude in disciplines like aerospace engineering, ocean engineering and structural engineering [7, 14, 15]. These exceptional features have motivated the development of different types of VINES models, such as single-sided VINES [16] with a single impact of attachment with the primary structure, hybrid VINES with the combination of both linear and nonlinear stiffness [17] and VINES with symmetric piecewise nonlinearities [10]. Recently, [18] proposed a TET mechanism where the advantages of both the NES with cubic stiffness and the impacting system have been utilised. The improved performance of the mechanism has also been validated with the experimental results.

The analysis of a VINES system is challenging as it exhibits non-smooth dynamics, typically requiring different approaches as compared to those used for smooth dynamical systems. For analytical investigation, most of the previous studies use multiple time scale methods [19, 20] with the mass ratio of the ball to the LO to be $\mathcal{O}(10^{-2})$. In [21], response regimes for optimal TET through

VINES, subjected to periodic excitation, are obtained analytically and experimentally. Also, an analytical method characterizes the chaotic dynamics of VINES by calculating the Lyapunov exponents and validating with the experimental results [22]. Recently, with a smaller mass ratio, Li *et al.* [2] proposed an electromagnetic VINES system which has improved TET via electrical damping. They demonstrate its application for both energy harvesting and vibration absorption. In another study [23], the effect of gravity and friction on the energy transfer through VINES is investigated numerically.

In a recent study [20], an asymptotic solution is proposed for VINES system for a light weight ball and for small excitation close to the resonant frequency. Analyses of VINES system with small parameters have been reported widely in the literature [4, 24, 25], providing tools to understand energy transfer in these regimes. However, less attention has been paid to the performance of VINES over a broad range of parameters relevant in many industrial/engineering applications. In [26], a semi-analytical map-based framework for the full VINES system captures the exact states of the system at consecutive impacts. The framework enables one to analytically obtain exact expressions for the complex periodic solution and perform the stability analysis. The analytical framework based on this exact solution enables one to remove the parametric limitations of previous analyses and accommodate any combination of parameter values in the analysis. This feature of the analysis is valuable, as straightforward simulations demonstrate the improved performance of TET with an increased mass ratio over a range of forcing frequencies, even for slightly increased forcing amplitudes.

With this motivation of improved TET performance over a larger range of parameters, the VINES model is considered for TET that absorbs vibrations from the primary structure. This VINES system consists of a ball of mass m moving without friction within a cavity of the LO having mass M and natural frequency ω_0. The LO is subjected to external excitation of frequency ω. In this study, the emphasis is on exploring the dynamics of the full VINES model for small to large values of m, for larger excitation amplitudes and for a broad spectrum of the excitation frequency. One focus of this paper is behavior that provides optimal TET as well as reduced oscillations of the LO, obtained by the periodic behavior with a pair of alternating impacts on either end of the cavity per forcing frequency. Using the recently developed semi-analytical map-based approach [26], we obtain analytical results in multiple parameter regimes for these periodic solutions and their stability. In particular, this analysis leads to the identification of mass ratios which yield efficient TET at $\omega = \omega_0$ as well as other frequency bands.

To better understand this phenomenon, we contrast this optimal behavior with resonance-like behavior for smaller values of forcing frequency. Given the passive nature of the VINES design, an alternating chattering behavior is observed for larger mass ratios, characterized by sequences of multiple impacts with small relative velocities that alternate between either end of the cavity. This chattering phenomenon is not desirable given the low relative impact velocities, appearing in regimes showing resonance-type behavior. While it is less prominent for parameter combinations with smaller values of η and F, consideration of a broader parameter range motivates a closer

study. The appearance of the alternating chatter for $\omega < \omega_0$ when m is non-negligible leads to an exploration of the shift in the peak response of the LO. While for smaller mass ratios ($\ll 1$) the effective mass of the system $M+m \approx M$, for larger mass ratios the sequence of repeated impacts on each end of the cavity effectively increases the mass of the system, and hence the natural frequency of the system (ω_s) is different from that of the LO (ω_0) at certain forcing frequencies away from ω_0. As a result, the TET may be more robust near the resonant frequency of the LO.

Given the full spectrum of efficient and inefficient TET observed over different parameter combinations, the objective of this study is to analyse the performance of VINES in vibration suppression through different energy transfer measures over a broad range of parameter values. Throughout, we use complementary numerical and analytical results to go beyond evaluation of the TET performance, providing a thorough understanding of the dynamical behaviors leading to the different outcomes. The numerically obtained parameter regimes for effective TET are validated with that obtained through the analytically obtained solutions and their stability analysis. As the map-based approach uses closed-form expressions, it is both robust as well as computationally efficient as compared to the numerical approach over relevant parameter regimes for periodic behavior. The analytical approach provides a comparison of relative and absolute (impact) velocities that deeply influence the TET in VINES. The approach also reveals certain types of preferred behavior in parameter regimes that may have been overlooked based on the numerical simulations. Therefore, this semi-analytical scheme provides an additional computationally efficient tool to the designer.

This paper is organized as follows: Section 2 discusses the mathematical modeling of the VINES system and the dimensionless form of the governing system of equations is presented. Section 2.1 defines the different energy transfer measures and discusses the results for small parameters of VINES. The analytical map-based approach obtained by solving the non-dimensional equations and linear stability analysis is reported in Section 3. Section 4 discusses the numerical results which are carried out for several combinations of large parameter values and supported by the analytical results. The salient outcomes of the study and the future directions are presented in Section 5.

2. Mathematical model

We consider a VINES model, consisting of a ball of mass (m) that travels without friction inside the cavity of length ($2L$) of a linear oscillator (LO) of mass (M). Here, the primary mass (M), attached to the base through a spring of stiffness (k) and a damper with damping coefficient (c), is subjected to an external excitation of the form ($x_s(t) = A\sin(\omega t + \varphi)$) as shown in Fig. 1. The motion of the LO and the ball between impact ($|x_m - x_b| < L$) is smooth and governed by

$$Mx_m''(t) + cx_m'(t) + kx_m(t) = kA\sin(\omega t + \varphi) + c\omega A\cos(\omega t + \varphi), \tag{1}$$

$$\ddot{x}_b = 0. \tag{2}$$

Here, $x_m(t), x_b(t)$ are the displacements of the mass (M) and the ball, respectively, at time t. The forcing frequency and phase difference are denoted by ω and φ, respectively. Also, if one

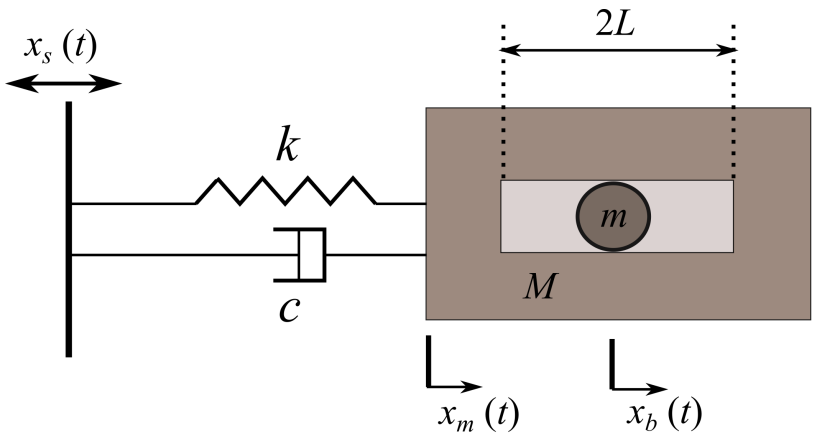

Figure 1: Schematic of VINES system where a ball of mass m oscillates inside the cavity of the LO of mass M.

is interested in the long-term behavior (steady state solution) of the system, then the choice of initial conditions becomes immaterial due to dissipation of transients in the absence of co-existing solutions. Moreover, at condition $|x_m - x_b| = L$, impacts between the ball and LO are governed by the instantaneous Newtonian impact law in conjunction with the conservation of momentum given by

$$x'_m{}^{+} - x'^{+}_b = -r(x'_m{}^{-} - x'^{-}_b) \tag{3}$$
$$Mx'_m{}^{+} + mx'^{+}_b = Mx'_m{}^{-} + mx'^{-}_b, \tag{4}$$

where, r denotes the coefficient of restitution. The superscripts $(\cdot)^-$ and $(\cdot)^+$ represent the variables before and after the impact respectively and $(\cdot)'$ indicates the derivative with respect to t.

Next, by introducing the dimensionless form of the displacement of the LO $z_m = \frac{x_m}{L}$ and the displacement of the ball $z_b = \frac{x_b}{L}$ where L is the half length of the cavity, Eqs. (1)-(4) can be rewritten in the non-dimensionalized form as,

$$\begin{aligned} |z_m - z_b| < 1: \quad & \ddot{z}_m + \eta\xi\dot{z}_m + z_m = F\sin(\Omega\tau + \varphi) + \eta\xi\Omega F\cos(\Omega\tau + \varphi) \\ & \ddot{z}_b = 0 \end{aligned} \tag{5}$$

$$\begin{aligned} |z_m - z_b| = 1: \quad & \dot{z}^+_m - \dot{z}^+_b = -r(\dot{z}^-_m - \dot{z}^-_b) \\ & \dot{z}^+_m + \eta\dot{z}^+_b = \dot{z}^-_m + \eta\dot{z}^-_b\,, \end{aligned} \tag{6}$$

where, $\dot{}$ denotes $\frac{d}{d\tau}$. The various dimensionless parameters used in this study are defined as,

$$\eta = \frac{m}{M}, \quad \Omega = \frac{\omega}{\omega_0}, \quad \omega_0 = \sqrt{\frac{k}{M}}, \quad \xi = \frac{c}{m\omega_0}, \quad F = \frac{A}{L}, \quad \tau = \omega_0 t, \quad \omega_s = \sqrt{\frac{k}{M(1+\eta)}}. \tag{7}$$

Here, ω_s denotes the natural frequency of the system which consists of the LO and the ball. It becomes important when the system exhibits alternate chattering-type dynamics for different combinations of system parameters.

In the following, the non-dimensional form of the governing equations mentioned in Eqs. (5)-(6) is used for the analysis and solved numerically using Runge-Kutta method. The impact time is calculated with an error of $\mathcal{O}(10^{-9})$. The system parameters utilized in this study are consistent with those specified in [26] as mentioned in Table 1.

Table 1: Numerical value of parameters of the VINES system used in the analysis.

System parameters	Value
Mass of LO (M)	3.807 kg
Length of the cavity ($2L$)	0.03 m
Coefficient of restitution (r)	0.65
Spring constant (k)	11680 N/m
Damping coefficient (c)	2.53 N-s/m

2.1. Energy transfer measures for TET

A number of measures are reported in the literature to quantify the energy transfer through the TET mechanism, see [21, 27–29] for details. Based on the measures considered in [26], in this study, two measures are used for quantifying the energy transfer (a) maximum (dimensional) displacement of the LO ($x_m^{\max}$) and (b) ratio of kinetic energy (KE), defined as

$$x_m^{\max} = L \times \max_{\mathcal{T}\in[0,7000]}(|z_m|) \quad \text{and} \quad \frac{K_b}{K_m + K_b} \text{ where } K_m = \left\langle \frac{1}{2} M \dot{z}_m^2 \right\rangle, \; K_b = \left\langle \frac{1}{2} m \dot{z}_b^2 \right\rangle, \tag{8}$$

where K_m, K_b and $\mathcal{T}$ denote the KE of the LO, KE of the ball and total simulation time, respectively. $\langle\cdot\rangle$ denotes the average operator. For accurate estimation of the average KE of the ball and the LO, a sufficiently large time history is considered. It has been observed that for the considered parameter values, the transients are short. Here, Eqs. (5)-(6) are solved for a non-dimensional time span of 7000 units and the last 3000 data are used for the measures in Eq. (8).

Figure 2 illustrates the effect of varying the mass ratio on energy transfer measures for (small) amplitude of forcing F, namely 0.05 and 0.1. It is evident from Figs. 2(a) and (b) that with the increase in F, *i.e.* with the increase in input energy to the system, the peak of the ratio of KE

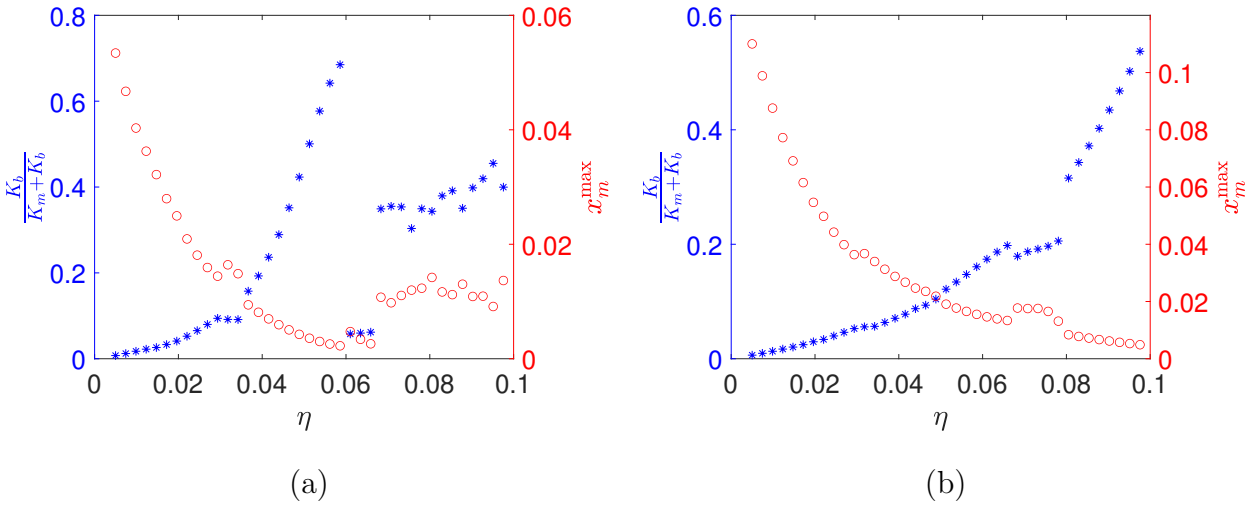

Figure 2: Quantification of energy transfer from the LO to the ball by estimating maximum displacement (red circle) of the LO (in m) and the ratio of KE of the ball to the total KE of the system (blue star) for different mass ratios when forcing amplitudes are (a) $F = 0.05$, (b) $F = 0.1$ and frequency ratio is $\Omega = 1$.

shifts towards the right and the maximum displacement of the LO is also increased as expected. Notably, Fig. 2 also highlights that when the energy transfer is maximum, the LO displacement is minimum, which is a desirable characteristic for a practical forced engineering systems. This observation suggests that for higher input energy, a ball with small inertia is not a suitable choice for efficient energy transfer. Consequently, these results serve as a foundation for further exploration of the effective TET in the context of larger mass ratio and forcing amplitude.

In order to gain further insights into the underlying mechanism for the effective TET through VINES for η between 0.04 and 0.06 in Fig. 2(a) and above 0.08 in Fig. 2(b), a bifurcation analysis is carried out as shown in Fig. 3. Figures 3(a) and (b) show the bifurcation diagram for the relative velocity $\dot{w}_i(= \dot{z}_{m,i} - \dot{z}_{b,i})$ at impacts as a function of the parameter η when F be 0.05 and 0.1, respectively. These figures provide noteworthy observations, indicating that when the system exhibits 1:1-periodic motion *i.e.*, two impacts in a forcing period [1], the ball effectively absorbs the energy of the LO and consequently reduces the displacement of the LO corresponding to those parametric regimes. Also, one can observe the secondary peaks in displacement for η values between 0.02 and 0.04 in Fig. 2(a) and between 0.06 and 0.08 in Fig. 2(b). These parameter ranges correspond to the transition from 2:1/1:2 solution, *i.e.*, two impacts on one side of the cavity and one impact on the other side in a forcing period [1], to the chaotic dynamics as evident from the bifurcation diagram shown in Fig. 3. As a consequence of this transition, energy transfer within the system decreases, resulting in an increase in the vibration amplitude of the LO.

Figures 4(a) and (c) present the time histories of both ends of the cavity of the LO and the

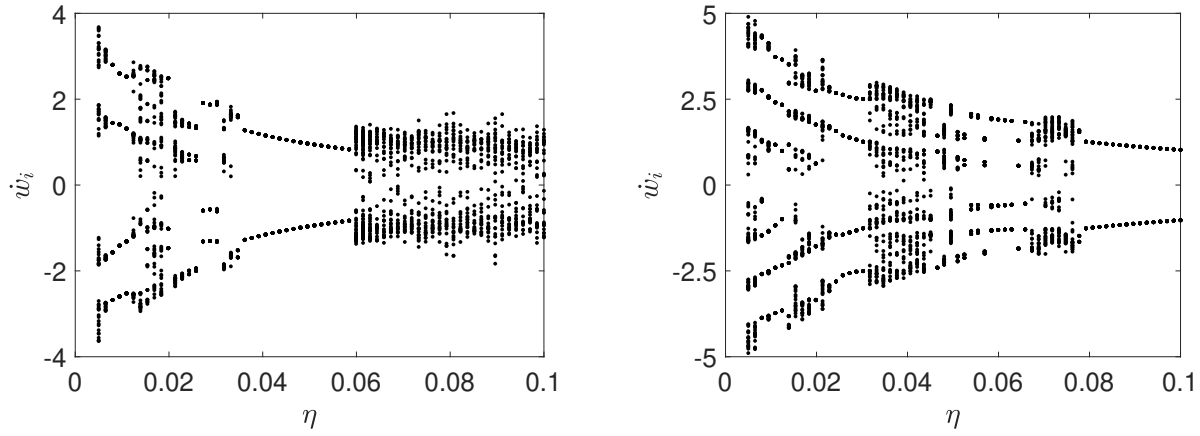

Figure 3: Bifurcation diagrams of the relative velocity of the system at impacts with respect to η for $\Omega = 1$ when (a) $F = 0.05$ and (b) $F = 0.1$.

ball for $\eta = 0.05$ corresponding to the periodic solution and $\eta = 0.085$ when the system exhibits complex dynamics. For the case when $\eta = 0.05$, the ball and the LO have regular impacts when they are moving in opposite directions. This behavior can be explained in terms of the impact phase, defined as

$$\varphi_i = \mathrm{mod}(\Omega\tau_i + \varphi, 2\pi), \tag{9}$$

where, τ_i denotes the impact time. Specifically, when $\varphi_i \in (0, \pi)$, both the ball and the LO move in the same direction at the right end of the cavity, while $\varphi_i \in (\pi, 2\pi)$ indicates out-of-phase motion, as shown in Fig. 4(a). This convention is consistent in the rest of the article. For $\eta = 0.05$, φ_i lies in the interval $(\pi, 2\pi)$ and hence results in efficient TET through VINES mechanism. On the other hand, for $\eta = 0.085$, the impacts are irregular, and consequently the energy transfer reduces as evident from Fig. 2(a). In fact, this phenomenon also results in increased relative velocity as can be seen in the phase planes shown in Figs. 4(b) and (d). Furthermore, when the ball strikes the LO as they are moving in the same direction with impact phase $\varphi_i < \pi$, as exemplified in Fig. 5(a)(for $\eta = 0.07$ and $F = 0.1$), the energy from the ball is transferred to the LO, resulting in the increased velocity of the LO which is not desirable for efficient TET. Consequently, the KE ratio decreases (Fig. 2(a)) and the relative velocity of the system increases. Likewise, the loss of periodicity in the impact between the ball and the LO, observed in Fig. 5(a), results in reduced energy transfer. For $\eta = 0.8$ and $F = 0.1$, where $\frac{K_b}{K_m+K_b}$ increases and $x_m^{\max}$ decreases further, the ball and the LO have regular impacts with $\varphi_i \in (\pi, 2\pi)$ as shown in Fig. 5(c). Consequently, the relative velocity reduces compared to the irregular impacts case as can be noticed in the phase planes in Figs. 5 (b) and (d).

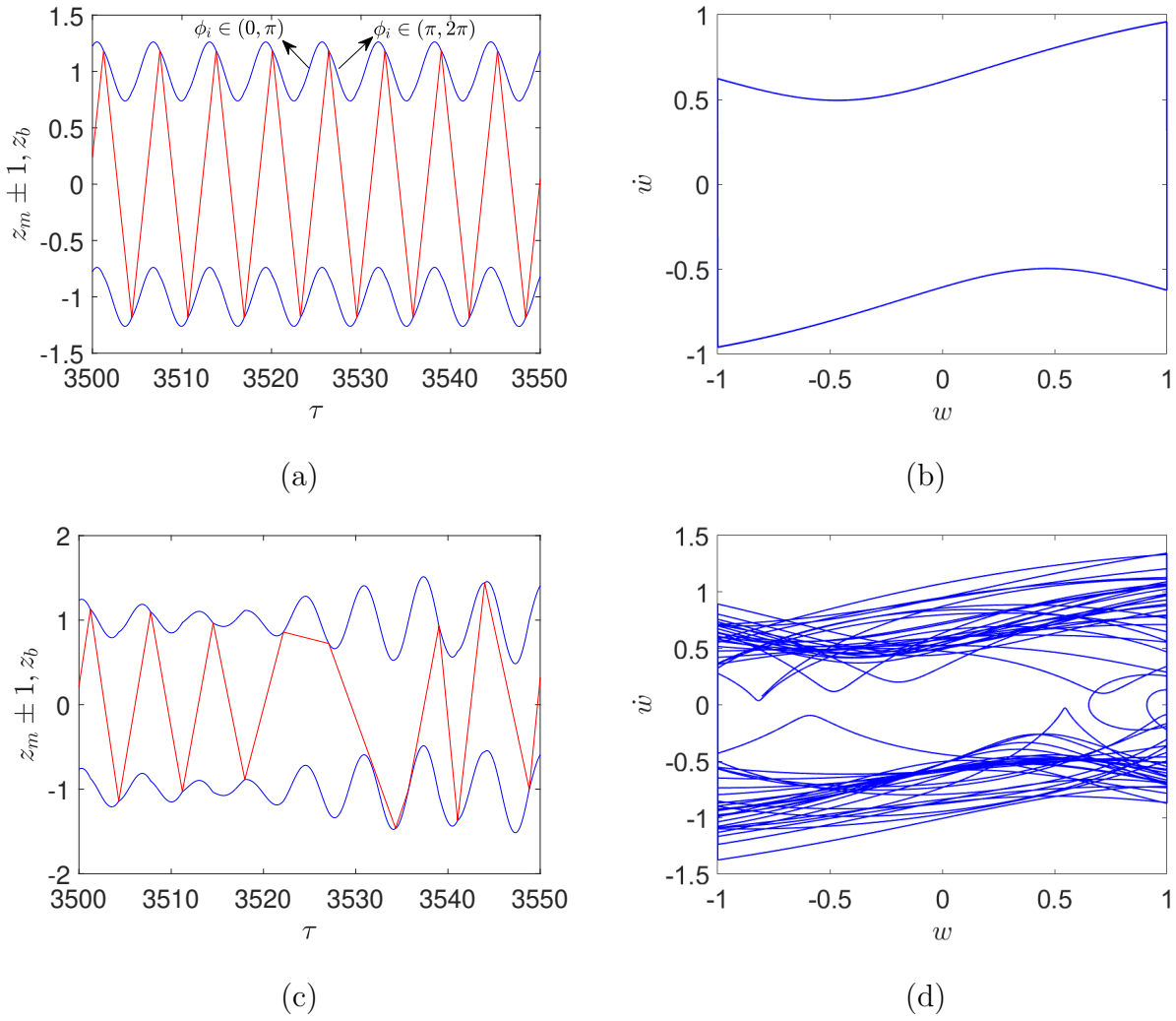

Figure 4: First column shows the time histories of the both ends of the cavity of the LO (blue line) and the ball (red line) when $F = 0.05$ for (a) $\eta = 0.05$ and (c) $\eta = 0.085$. Second column, (b) and (d), shows the phase portraits of the system corresponding to the parameters in (a) and (c), respectively. Here, $\Omega = 1$ and $r = 0.65$.

These results emphasize the significance of 1:1-periodic solution, with regular alternating impacts at both ends of the cavity, as being conducive to achieving effective TET through the VINES mechanism. Additionally, the impact phase $\varphi_i \in (\pi, 2\pi)$ at the right end of the cavity, implies the LO and the ball are moving in opposite directions, which results in reduced relative impact velocity. On the other hand, when the system exhibits chaotic dynamics, the impacts become irregular and also the impact phase at the right end of the cavity can fall outside $(\pi, 2\pi)$. This situation undermines the effectiveness of VINES in facilitating efficient energy transfer.

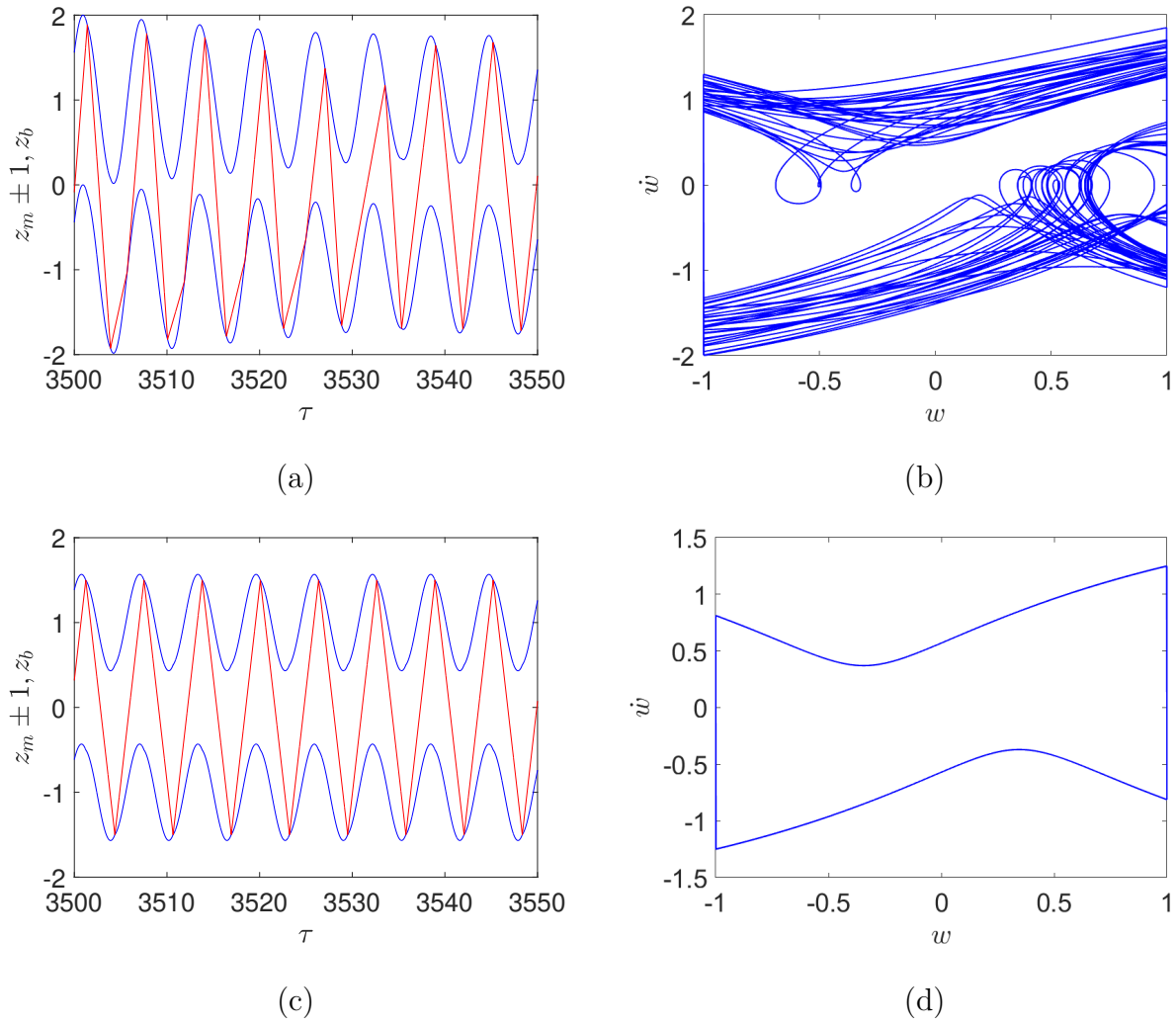

Figure 5: First column shows the time histories of the both ends of the cavity of the LO (blue line) and the ball (red line) when $F = 0.1$ for (a) $\eta = 0.07$ and (c) $\eta = 0.08$. Second column, (b) and (d), shows the phase portraits of the system corresponding to the parameters in (a) and (c), respectively. Here, $\Omega = 1$ and $r = 0.65$.

3. Map based analytical framework

Earlier studies use analytical approaches based on asymptotics, such as the method of multiple time scales, to study the VINES system whose accuracy requires significantly small mass ratio ($\eta \equiv \mathcal{O}(10^{-2})$) [30, 31]. These methods have been shown to be accurate for these reduced systems when $\Omega \approx 1$ and A is small. However, in a recent study, Liu *et al.* [26] has proposed a framework, based on the exact solution of the governing equations, which essentially liberates the analysis from

the aforementioned constraints associated with small system parameters. We review this framework, which provides flexibility in selecting the parameters and can be used for studying the dynamics of VINES for larger A, η and forcing frequencies Ω other than 1.

To define the maps from the present state at impact to the future impact, information of state variables at the impact is being used. Here, $z^-_{j,i}, z^+_{j,i}(\dot{z}^-_{j,i}, \dot{z}^+_{j,i})$ denotes the displacement (velocity) of the mass $j = m, b$ immediately before and after the i^{th} impact, respectively. τ_i is the time of the i^{th} impact. The impact conditions in Eq. (6) can be rewritten, using the continuity in displacement at impact, as

$$\begin{aligned} z^-_{j,i} &= z^+_{j,i} \quad j = m, b, \quad z_{m,i} - z_{b,i} = 1(-1) \quad \text{on} \quad \mathcal{L}(\mathcal{R}) \\ \dot{z}^+_{m,i} &= \tfrac{1-r\eta}{1+\eta}\dot{z}^-_{m,i} + \tfrac{\eta(1+r)}{1+\eta}\dot{z}^-_{b,i}, \quad \dot{z}^+_{b,i} = \tfrac{1+r}{1+\eta}\dot{z}^-_{m,i} + \tfrac{\eta-r}{1+\eta}\dot{z}^-_{b,i}, \end{aligned} \tag{10}$$

where, $\mathcal{L}$ and $\mathcal{R}$ denote the left and right end of the cavity. For the sake of convenience, the state of the system before the i^{th} impact is defined using a vector $\mathbf{s}_i$ as

$$\mathbf{s}_i = (z_{m,i}, \dot{z}_{m,i}, z_{b,i}, \dot{z}_{b,i}, \tau_i), \tag{11}$$

where, $z_{j,i} \equiv z^-_{j,i}$ and $\dot{z}_{j,i} \equiv \dot{z}^-_{j,i}$.

Now, to derive the maps from impact to impact, the set of linear differential equations (DEs) mentioned in Eq. (5) are solved and an explicit solution is obtained for $z^-_{j,i}$, $\dot{z}^-_{j,i}$ in terms of $z^+_{j,i-1}$, $\dot{z}^+_{j,i-1}$ for $j = m, b$. The expressions in Eq. (10) allow us to write in terms of $z^-_{j,i-1}$, $\dot{z}^-_{j,i-1}$ only. Hence, the superscript "$-$" is dropped in Eq. (11) and also in the rest of the discussions. By solving the DEs in Eq. (5), one obtains the displacement and velocity of the LO and the ball as

$$\begin{aligned} z_{m,i} &= p_{1,i-1}e^{-\frac{\eta\xi\tau_i}{2}}\sin(\alpha\tau_i) + p_{2,i-1}e^{-\frac{\eta\xi\tau_i}{2}}\cos(\alpha\tau_i) + q_1\sin(\Omega\tau_i+\varphi) + q_2\cos(\Omega\tau_i+\varphi) \\ &\equiv \mathcal{P}(\tau_{i-1}, \tau_i, z_{m,i-1}, \dot{z}_{m,i-1}, \dot{z}_{b,i-1}, \varphi) \end{aligned} \tag{12}$$

$$\begin{aligned} \dot{z}_{m,i} &= p_{1,i-1}e^{-\frac{\eta\xi\tau_i}{2}}\left(-\frac{\eta\xi}{2}\sin(\alpha\tau_i) + \alpha\cos(\alpha\tau_i)\right) + p_{2,i-1}e^{-\frac{\eta\xi\tau_i}{2}}\left(-\frac{\eta\xi}{2}\cos(\alpha\tau_i) - \alpha\sin(\alpha\tau_i)\right) \\ &\quad + q_1\Omega\cos(\Omega\tau_i+\varphi) - q_2\Omega\sin(\Omega\tau_i+\varphi) \\ &\equiv \mathcal{Q}(\tau_{i-1}, \tau_i, z_{m,i-1}, \dot{z}_{m,i-1}, \dot{z}_{2,i-1}, \varphi), \end{aligned} \tag{13}$$

$$z_{b,i} = z_{b,i-1} + \left(\frac{1+r}{1+\eta}\dot{z}_{m,i-1} + \frac{\eta-r}{1+\eta}\dot{z}_{b,i-1}\right)(\tau_i - \tau_{i-1}) \tag{14}$$

$$\dot{z}_{b,i} = \frac{1+r}{1+\eta}\dot{z}_{m,i-1} + \frac{\eta-r}{1+\eta}\dot{z}_{b,i-1}. \tag{15}$$

where, $\alpha = \sqrt{1 - \frac{(\eta\xi)^2}{4}}$. The constants $p_{1,i-1}$ and $p_{2,i-1}$ are dependent on impact time, displacement of the LO, velocities of the LO and the ball and the phase as indicated by the arguments of functions

$\mathcal{P}$ and $\mathcal{Q}$. They are obtained as follows,

$$q_1 = \frac{F(1-\Omega^2)+F(\eta\xi\Omega)^2}{(\eta\xi\Omega)^2+(1-\Omega^2)^2}, \quad q_2 = \frac{-F\eta\xi\Omega^3}{(\eta\xi\Omega)^2+(1-\Omega^2)^2}, \tag{16}$$

$$e^{-\frac{\eta\xi\tau_{i-1}}{2}} \begin{bmatrix} \sin(\alpha\tau_{i-1}) & \cos(\alpha\tau_{i-1}) \\ -\frac{\eta\xi}{2}\sin(\alpha\tau_{i-1}) + \alpha\cos(\alpha\tau_{i-1}) & -\alpha\sin(\alpha\tau_{i-1}) - \frac{\eta\xi}{2}\cos(\alpha\tau_{i-1}) \end{bmatrix} \begin{bmatrix} p_{1,i-1} \\ p_{2,i-1} \end{bmatrix} =$$

$$\begin{bmatrix} z_{m,i-1} \\ \frac{1-r\eta}{1+\eta}\dot{z}_{m,i-1} + \frac{\eta(1+r)}{1+\eta}\dot{z}_{b,i-1} \end{bmatrix} - \begin{bmatrix} \sin(\Omega\tau_{i-1}+\varphi) & \cos(\Omega\tau_{i-1}+\varphi) \\ \Omega\cos(\Omega\tau_{i-1}+\varphi) & -\Omega\sin(\Omega\tau_{i-1}+\varphi) \end{bmatrix} \begin{bmatrix} q_1 \\ q_2 \end{bmatrix}. \tag{17}$$

Now, Eqs. (12)-(15) are used to obtain $\mathbf{s}_i$ from $\mathbf{s}_{i-1}$, which require the information about τ_i in conjunction with the impact conditions which are

$$z_{m,l} - z_{b,l} = \pm 1, \quad \forall\ l > 0, l \in N. \tag{18}$$

In order to differentiate between various behaviors, we introduced four different maps P_p which govern the transition $\mathbf{s}_{i-1} \to \mathbf{s}_i$ and defined as

$$P_1 : \mathbf{s}_{i-1} \to \mathbf{s}_i \ \text{ for } \ \mathcal{L} \mapsto \mathcal{R}, \quad P_2 : \mathbf{s}_{i-1} \to \mathbf{s}_i \ \text{ for } \ \mathcal{R} \mapsto \mathcal{L} \tag{19}$$

$$P_3 : \mathbf{s}_{i-1} \to \mathbf{s}_i \ \text{ for } \ \mathcal{L} \mapsto \mathcal{L}, \quad P_4 : \mathbf{s}_{i-1} \to \mathbf{s}_i \ \text{ for } \ \mathcal{R} \mapsto \mathcal{R}. \tag{20}$$

It should be noted that the Eq. (18) differentiates the maps P_p. For example, for P_1 and P_4, $z_{m,i} - z_{b,i} = -1$ and $z_{m,i-1} - z_{b,i-1} = 1(-1)$ for $P_1(P_4)$. Similarly, for P_2 and P_3, $z_{m,i} - z_{b,i} = 1$ and $z_{m,i-1} - z_{b,i-1} = -1(1)$ for $P_2(P_3)$. Here, these maps serve as building blocks to analyse the different periodic solutions of the system. Next, the analytical expressions for the case of 1:1-periodic solutions based on these maps are presented.

3.1. 1:1 periodic solutions

When the ball impacts alternately at either end of the LO in one forcing period T, one obtains the 1:1-periodic solution such that $\mathbf{s}_{i-1} = \mathbf{s}_{i+1}$ with the periodicity conditions

$$\tau_{i+1} - \tau_{i-1} = T, \quad z_{j,i-1} = z_{j,i+1} \ \text{ and } \ \dot{z}_{j,i-1} = \dot{z}_{j,i+1}, \tag{21}$$

where, $j = m, b$. The 1:1 periodic solution can be described as $P_2(P_1(s_{i-1})) = s_{i+1}$ using the maps. Here, $P_1(s_{i-1}) = s_i$. Now, the unknown state variables $(z_{m,l}, \dot{z}_{m,l}, \dot{z_{b,l}}, t_l); l = i, i+1$ at either end of the cavity need to be determined by solving the system of equations obtained through Eqs. (12)-(15)

along with Eq. (18). The desired system of equations in terms of $\mathbf{s}_{i-1}$ is given as

$$
\begin{aligned}
z_{m,i} &\equiv \mathcal{P}(\tau_{i-1}, \tau_i, z_{m,i-1}, \dot{z}_{m,i-1}, \dot{z}_{b,i-1}, \varphi),\\
\dot{z}_{m,i} &\equiv \mathcal{Q}(\tau_{i-1}, \tau_i, z_{m,i-1}, \dot{z}_{1,i-1}, \dot{z}_{2,i-1}, \varphi),\\
z_{b,i} &= z_{b,i-1} + \left(\frac{1+r}{1+\eta}\dot{z}_{m,i-1} + \frac{\eta-r}{1+\eta}\dot{z}_{b,i-1}\right)(\tau_i - \tau_{i-1}),\\
\dot{z}_{b,i} &= \frac{1+r}{1+\eta}\dot{z}_{m,i-1} + \frac{\eta-r}{1+\eta}\dot{z}_{b,i-1},
\end{aligned} \tag{22}
$$

$$
z_{m,i} - z_{b,i} = -1, \quad z_{m,i-1} - z_{b,i-1} = 1, \tag{23}
$$

$$
\begin{aligned}
z_{m,i+1} &\equiv \mathcal{P}(\tau_i, \tau_{i+1}, z_{m,i}, \dot{z}_{m,i}, \dot{z}_{b,i}, \varphi),\\
\dot{z}_{m,i+1} &\equiv \mathcal{Q}(\tau_i, \tau_{i+1}, z_{m,i}, \dot{z}_{m,i}, \dot{z}_{b,i}, \varphi),\\
z_{b,i+1} &= z_{b,i} + \left(\frac{1+r}{1+\eta}\dot{z}_{m,i} + \frac{\eta-r}{1+\eta}\dot{z}_{b,i}\right)(\tau_{i+1} - \tau_i),\\
\dot{z}_{b,i+1} &= \frac{1+r}{1+\eta}\dot{z}_{m,i} + \frac{\eta-r}{1+\eta}\dot{z}_{b,i},
\end{aligned} \tag{24}
$$

$$
\tau_{i+1} = \tau_{i-1} + T. \tag{25}
$$

Here, $\mathbf{s}_{i+1}$ in Eq. (24) is written in terms of $\mathbf{s}_{i-1}$ by substituting s_i from the Eq. (22) and using the periodicity condition, these equations are solved for $\mathbf{s}_{i-1}$ and subsequently for $\mathbf{s}_i$. Also, for the sake of convenience, τ_{i-1} can be assumed to be 0 for solving the system of equations. For the symmetric 1:1-periodic solution, $\Delta\tau_{i-1} = \Delta\tau_i$, defined as

$$
\Delta\tau_{i-1} = \tau_i - \tau_{i-1}, \quad \Delta\tau_i = \tau_{i+1} - \tau_i, \tag{26}
$$

where τ_i denotes the time at the i^{th} impact, otherwise the solution is asymmetric. It is also important to analyse the stability of the obtained periodic solution which will be discussed in the subsequent section.

3.2. Linear stability analysis

The stability of the 1:1-periodic solution governs the effective and consistent energy transfer through VINES system. In this study, the linear stability analysis of the 1:1 periodic solution is found by considering small perturbations to the fixed points of the system. Here, the fixed points for the composite map $P_2 \circ P_1$ are $\mathbf{s}_1^*$ and $\mathbf{s}_2^*$ which denote the state of the system during impact

at the left and right ends of the cavity, respectively. The system is linearized about $\delta s_h = 0$, where $h = i-1, i, i+1$ and this linearization results in $[\delta \mathbf{s}_{i+1} \approx J_{P_2}(\mathbf{s}_2^*) J_{P_1}(\mathbf{s}_1^*) \delta \mathbf{s}_{i-1}]$; see [26] for mathematical details. Here, $J_{P_p} \in \Re^{4\times 4}$, where $p = 1, 2$, denote the Jacobian matrices for P_1 and P_2. The state variable z_m can be obtained from z_b by using Eq. (23) and therefore, J_{P_p} can be obtained as

$$J_{P_p} = \begin{bmatrix} \frac{\partial \dot{z}_{m,i-1+p}}{\partial \dot{z}_{m,i-2+p}} & \frac{\partial \dot{z}_{m,i-1+p}}{\partial \dot{z}_{b,i-2+p}} & \frac{\partial \dot{z}_{m,i-1+p}}{\partial z_{b,i-2+p}} & \frac{\partial \dot{z}_{m,i-1+p}}{\partial \tau_{i-2+p}} \\ \frac{\partial \dot{z}_{b,i-1+p}}{\partial \dot{z}_{m,i-2+p}} & \frac{\partial \dot{z}_{b,i-1+p}}{\partial \dot{z}_{b,i-2+p}} & \frac{\partial \dot{z}_{b,i-1+p}}{\partial z_{b,i-2+p}} & \frac{\partial \dot{z}_{b,i-1+p}}{\partial \tau_{i-2+p}} \\ \frac{\partial z_{b,i-1+p}}{\partial \dot{z}_{m,i-2+p}} & \frac{\partial z_{b,i-1+p}}{\partial \dot{z}_{b,i-2+p}} & \frac{\partial z_{b,i-1+p}}{\partial z_{b,i-2+p}} & \frac{\partial z_{b,i-1+p}}{\partial \tau_{i-2+p}} \\ \frac{\partial \tau_{i-1+p}}{\partial \dot{z}_{m,i-2+p}} & \frac{\partial \tau_{i-1+p}}{\partial \dot{z}_{b,i-2+p}} & \frac{\partial \tau_{i-1+p}}{\partial z_{b,i-2+p}} & \frac{\partial \tau_{i-1+p}}{\partial \tau_{i-2+p}} \end{bmatrix}. \tag{27}$$

Each of the partial derivatives in Eq. (27) can be obtained numerically, however, in this study these have been obtained through implicit differentiation of Eqs. (12) - (15) whose expressions can be found in the Appendix A. For a stable solution, the modulus of the eigenvalues (λ's) of the matrix $J_{P_2}(\mathbf{s}_2^*) J_{P_1}(\mathbf{s}_1^*)$ are less than unity, otherwise the solution is unstable.

Remark: Commonly used techniques in the study of stability of a periodic solution include those based on Poincàre sections [32] and Floquet theory [33, 34]. In particular, a Floquet theory based approach requires the computation of monodromy matrix (Φ), a state transition matrix, which maps the state of the system at $\tau = 0$ to its state after one forcing period T of a smooth dynamical system. Notably, for non-smooth systems, the calculation of the monodromy matrix for a dynamical system with impacting surfaces involves the calculation of saltation matrix (S) which maps the state of the system before an impact, e.g. $(z_m^-, \dot{z}_m^-, z_b^-, \dot{z}_b^-)$, to that after the impact, e.g. $(z_m^+, \dot{z}_m^+, z_b^+, \dot{z}_b^+)$. Previous studies of non-autonomous systems using Floquet theory typically define the state vector in terms of displacement and velocity, with the monodromy matrix $\Phi = S_2 \cdot A_2 \cdot S_1 \cdot A_1$ for a solution with the impacting sequence $\mathcal{L} \to \mathcal{R} \to \mathcal{L}$, where A_1 and A_2 denote the state transition matrices from the left impacting surface (at $\tau = 0$) to the right impacting surface and from the right impacting surface to the left one (at $\tau = T$), respectively, while S_1 and S_2 are the saltation matrices corresponding to the impact dynamics at the right and left surfaces, respectively. For example, a recent study [34] considered this formulation, showing that higher order approximations in the Taylor series expansion of the state vector at impact improves the accuracy of the calculated impact time substantially, compared to a linear approximation.

In contrast, our study incorporates time τ as one of the state variables, resulting in the state vector $\mathbf{s}_i$ as mentioned in Eq. (11), which is described by a nonlinear system of equations, given by Eqs. (22)-(25), for the transitions $\mathcal{L} \to \mathcal{R}$ and $\mathcal{R} \to \mathcal{L}$. A saltation matrix S could be computed using the impact conditions as mentioned in Eq. (10). However, given the (linear) simplicity of these conditions, we substitute Eq. (10) directly into Eqs. (12)-(15). Then, we have an exact nonlinear map $P_2 \circ P_1$, which gives the system of Eqs. (22)-(25), between the state variables before impact

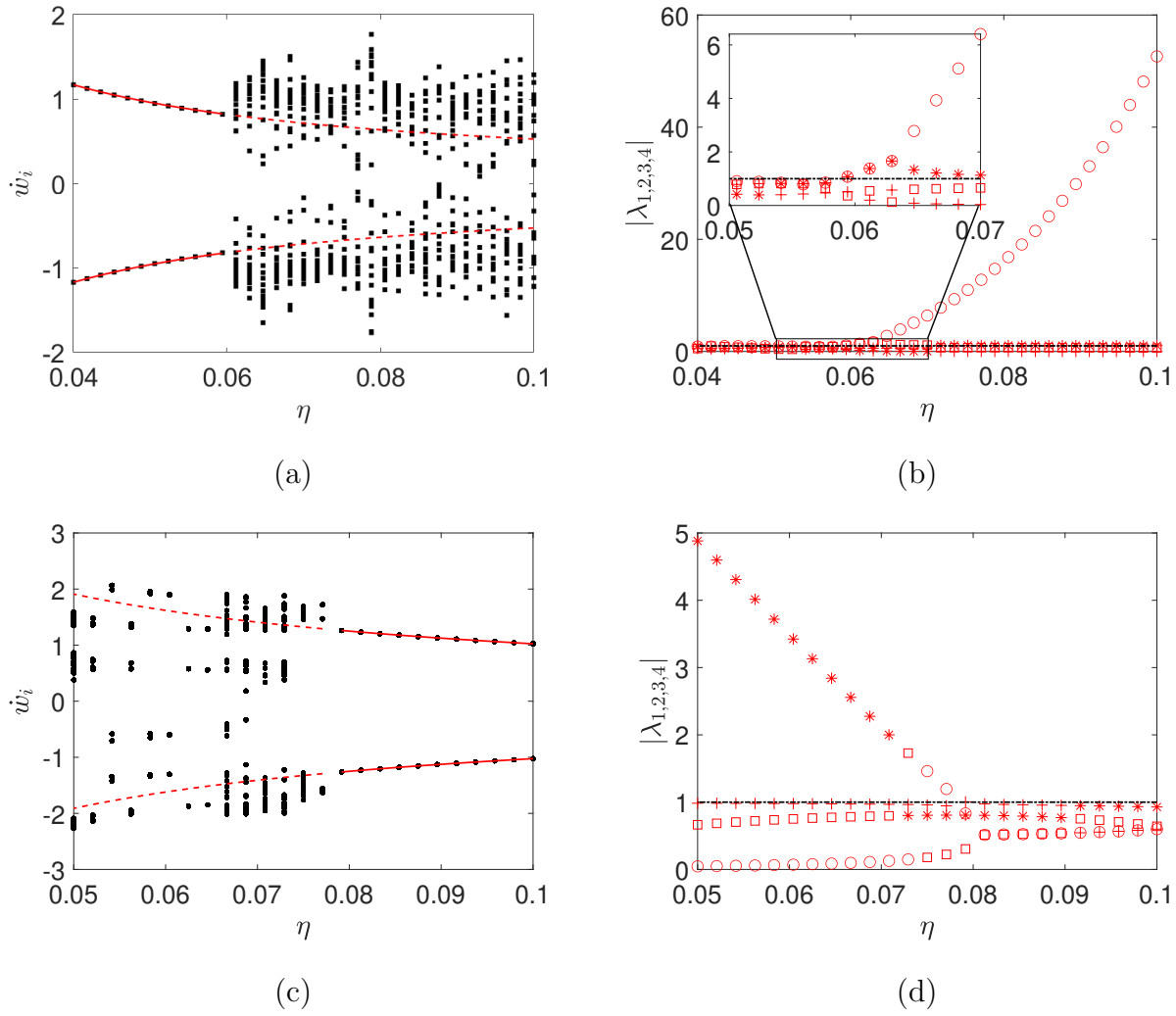

Figure 6: First column shows the zoomed version of the bifurcation diagrams shown in Fig. 3. Black dots and red line represent the numerical and analytical results, respectively. Last column, (b) and (d), shows the effect on absolute value of the eigenvalues of $J_{P_2}J_{P_1}$ with respect to η. The dotted black line corresponds to $|\lambda| = 1$ for the reference.

only $(z_m^-, \dot{z}_m^-, z_b^-, \dot{z}_b^-, \tau)$. Then, the matrix $J_{P_2}(\mathbf{s}_2^*)J_{P_1}(\mathbf{s}_1^*)$ describes the local effects of perturbations to this nonlinear map.

Utilizing the map based approach, as discussed above, the analytical 1:1 periodic solution is obtained as shown with red circle in the zoomed Figs. 6(a) and (c). It is evident from the Figs. 6(a) and (c) that the analytical results obtained for the 1:1 periodic solution show an excellent match with that obtained through the numerical analyses (black dots). Please note that the numerical

bifurcation branches are obtained by continuation approach; *i.e.*, for a given η, Eqs. (5)-(6) are simulated for a longer time interval to obtain an attracting solution which is subsequently used as an initial condition in the next iteration (typically for a nearby η value). Here, the analytical results consist of both stable and unstable solutions as depicted in Figs 6(a) and (c) with solid red and dotted red lines. It can be observed that the absolute value of eigenvalues become greater than unity for $\eta \gtrapprox 0.06$ in Fig. 6(b) and for $\eta \lessapprox 0.08$ in Fig. 6(d), indicating the unstable solutions. An inset in Fig. 6(d) is provided which shows that the $|\lambda|'s$ are less than unity for $\eta \lessapprox 0.06$ and hence the corresponding solutions are stable. It can also be observed in Figs. 6(b) and (d) that one of the eigenvalues is in close proximity to unity suggesting that the long time dynamics of the solution could be sensitive to stochastic excitation.

4. VINES over a larger parameter range

The result presented in Fig. 2 clearly indicate that increasing the inertia of the ball essentially enhances the effectiveness of TET mechanism particularly for the higher forcing amplitude when $\Omega = 1$. This observation serves as motivation to extend this investigation of TET through VINES for higher values of η and F. Additionally, it is essential to analyse the system for large parameter values with Ω other than unity which typically replicate the more realistic engineering problems. These aspects will be discussed in detail in the subsequent section.

This section, in contrast to the earlier studies, considers the cases where amplitude of excitation is not necessarily small, as well as values of m over a range of percentage of M. Also, we examine the effect of excitation frequency, which may not always be close to ω_0. To investigate the influence of excitation amplitude and mass ratio on the TET through VINES, we present contour plots in Fig. 7 for different frequency ratios. Notably, as the frequency ratio Ω increases, the yellow region (indicating the maximum value of the KE ratio) also expands, signifying the effective TET over a wide range of parameter values in the $\eta - F$ plane. To provide further insights, sectional views of the results in Fig.7 corresponding to different F are presented in Fig. 8. These sectional views reveal that the maximum displacement of the LO coincides with the regions where the KE ratio is low. Figure. 7(d) reveals that the peak response of the LO is attained when $\eta \approx 0.22$ for $\Omega = 0.9$, which is also evident from Figs. 8(a) and (d). An additional noteworthy observation is the persistent presence of the yellow region, indicating efficient TET, particularly for $\Omega \geq 1$ along the diagonal where $\eta \approx F$. The bifurcation analysis, shown in Fig. 14, highlights these parameter sets, where the system exhibits the corresponding 1:1-periodic dynamics. It can be seen here that for appropriate parametric combinations the KE ratio is more than 70% with reduced x_m^{max} which reflects the efficient performance of VINES. On the other hand, the bifurcation analysis presented in Fig. 14 reveals that the VINES system exhibits low KE ratio (blue regions in Figs. 7(a)-(c)) for parameter values corresponding to chaotic dynamics.

In this study $\eta \equiv \mathcal{O}(1)$ which affects the natural frequency of the system (ω_s) when it exhibits alternating chatter. When $\eta \ll 1$, $\omega_s \approx \omega_0$ results in the peak response when $\Omega \approx 1$. This scenario

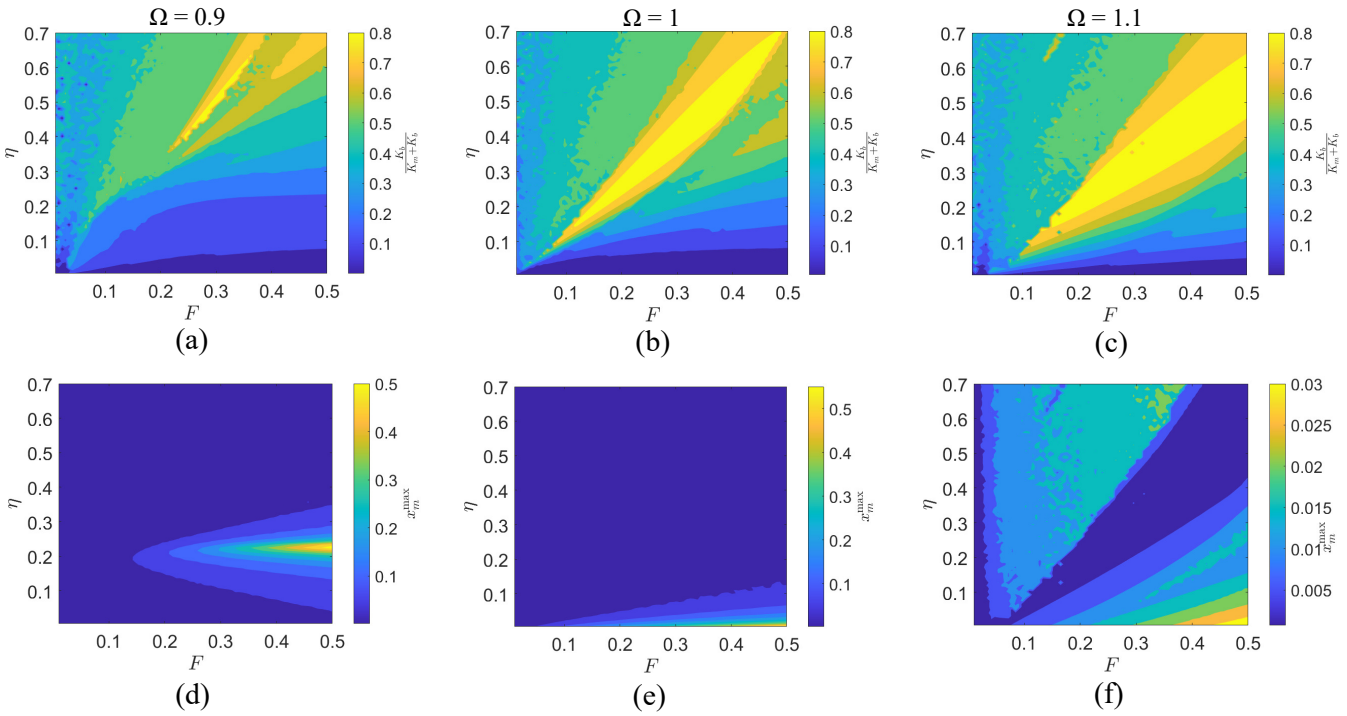

Figure 7: Effect of non-dimensional amplitude of forcing F and varying mass ratio η on the ratio of KE of the ball and the total KE of the system and on the maximum displacement of the LO. First column, (a) and (d), corresponds to $\Omega = 0.9$; second column, (b) and (e), corresponds to $\Omega = 1$; last column, (c) and (f), corresponds to $\Omega = 1.1$.

has been extensively discussed in the previous studies. However, in this study, we focus on the case when the mass ratio $\eta \equiv \mathcal{O}(1)$. On account of the ball of significant mass, the overall mass of the system increases,resulting in a decrease in the natural frequency of the system, as depicted by the dashed pink line in Figs. 12(a)-(c). Therefore, at $\eta \approx 0.22$, the natural frequency of the system (ω_s) becomes very close to the forcing frequency (ω) when $\Omega = 0.9$ leading to the maximum response. It can be seen in Fig. 8 that the peaks of the maximum displacement and the KE ratio are shifting towards lower values of η as the frequency ratio Ω is increasing and has been discussed in detail in Subsection 4.2.

Also, it can be inferred from Fig. 2(a) that the performance of VINES has improved for η varying between 0.04 to 0.06. For the corresponding parameter values, the system exhibits 1:1 periodic dynamics as shown in the bifurcation diagram of Fig. 3(a). The time histories shown in Figs. 4 and 5 emphasize that efficient energy transfer through VINES is achieved for 1:1 periodic solutions when the ball hits the LO out-of-phase with the forcing. In the subsequent section, we investigate the effect of impact phase on energy transfer and its relationship to 1:1 periodic solutions for larger parameter regimes.

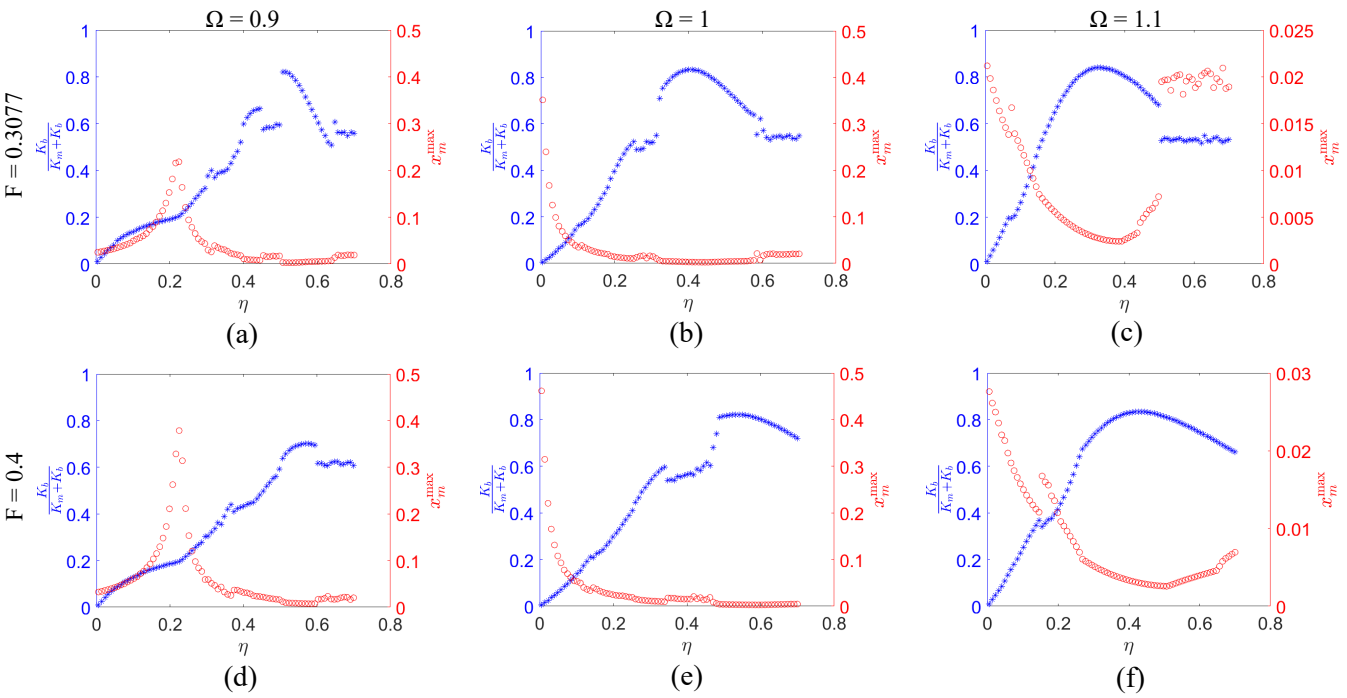

Figure 8: Sectional view of the contour plots shown in Fig. 7 for $\Omega = 0.9, 1$ and 1.1 (left to right) when $F = 0.3077$ (top row) and $F = 0.4$ (bottom row).

4.1. Influence of impact phase

It is worth noting that the impact phase $\varphi_i < \pi$ between the ball and the LO is not conducive to effective TET. The time-series, shown in Figs. 9 and 10, of the (non-dimensional) displacement of the ball and the LO shows different cases of impact phase for various parameter combinations of the system. In Fig. 9, we consider a couple of cases when $\Omega < 1$: $\omega < \omega_s$ and $\omega \approx \omega_s$. In the first case, where $\Omega = 0.8$, the ball impacts twice the LO at either end. For the first impact, the impact phase $\varphi_i < \pi$, while for the second impact, the impact phase φ_i falls in the interval $(\pi, 2\pi)$. However, for the same set of parameters ($\eta = 0.2$, $F = 0.4$) at $\Omega = 0.9$, the system exhibits chattering behavior with repeated impacts having negligible relative impact velocities as indicated by the phase plane in Fig. 9(d). In fact, at $\Omega = 0.9$ for $\eta = 0.2$, the system exhibits chattering behavior leading to an amplified response of the LO and thus an inefficient TET mechanism.

On the other hand, at $\omega \approx \omega_s$, time series plots and phase planes in Figs. 10(a)-(d), corresponding to Figs. 8(e) and (f) where $\frac{K_b}{K_m+K_b}$ is large, illustrate an out-of-phase 1:1 periodic behaviour of the system with $\varphi_i \in (\pi, 2\pi)$ which essentially helps in vibration attenuation. Additionally, Figure 7 demonstrates that the frequency ratio Ω is another important parameter that significantly influences the effective TET through VINES, which will be investigated in the subsequent analysis

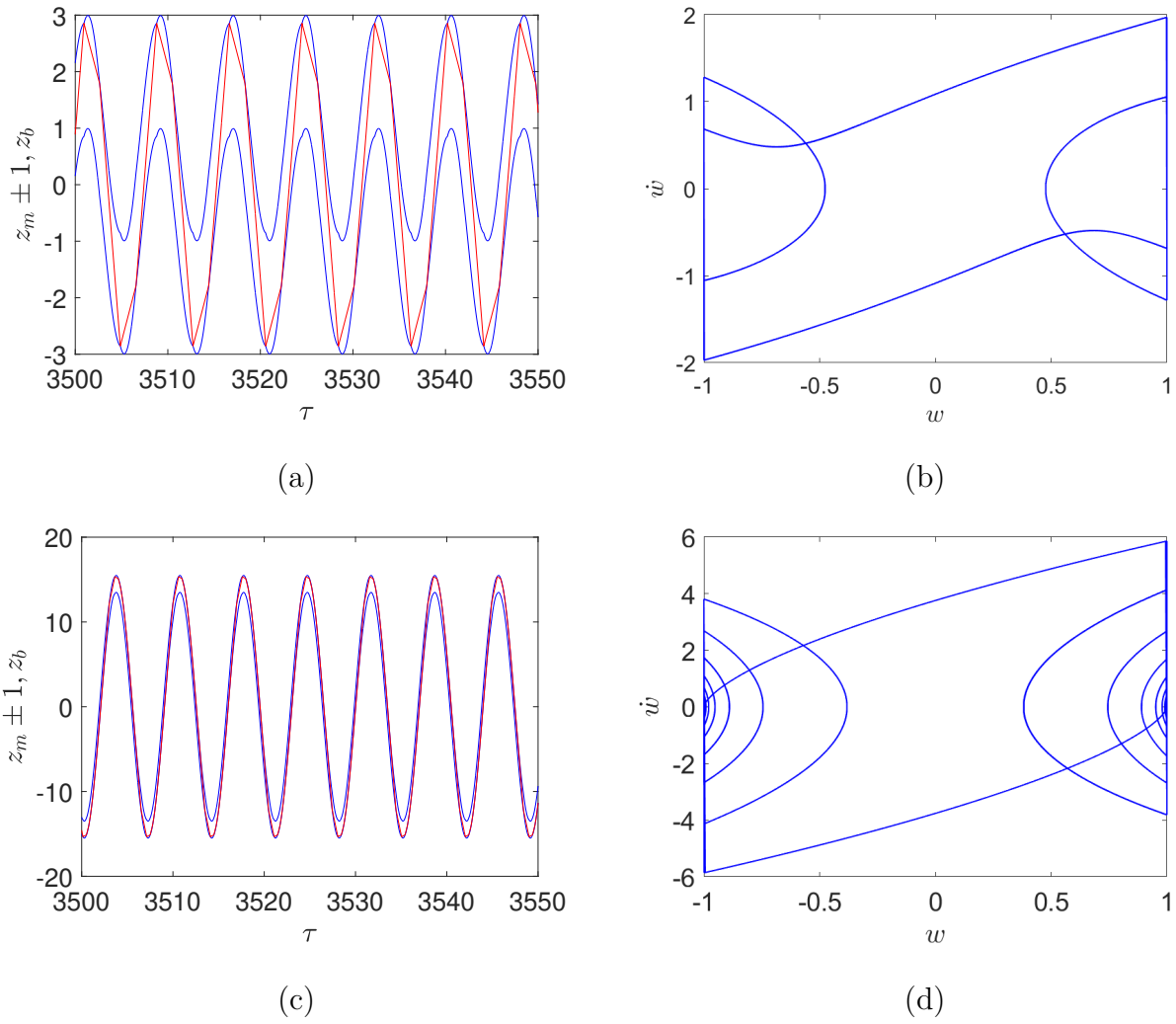

Figure 9: Time history (first column) of the non-dimensional displacement of the LO and the ball and the corresponding phase portrait (second column) of the system when amplitude of excitation is $F = 0.4$ and $\eta = 0.2$. The first row corresponds to $\Omega = 0.8$ (here, $\omega < \omega_s$ for $\eta = 0.2$) and for the second row $\Omega = 0.9$. The second row reveals the alternating chatter phenomenon, resulting in large amplitude of oscillations, with sequences of small relative impact velocities.

in Subsection 4.2.

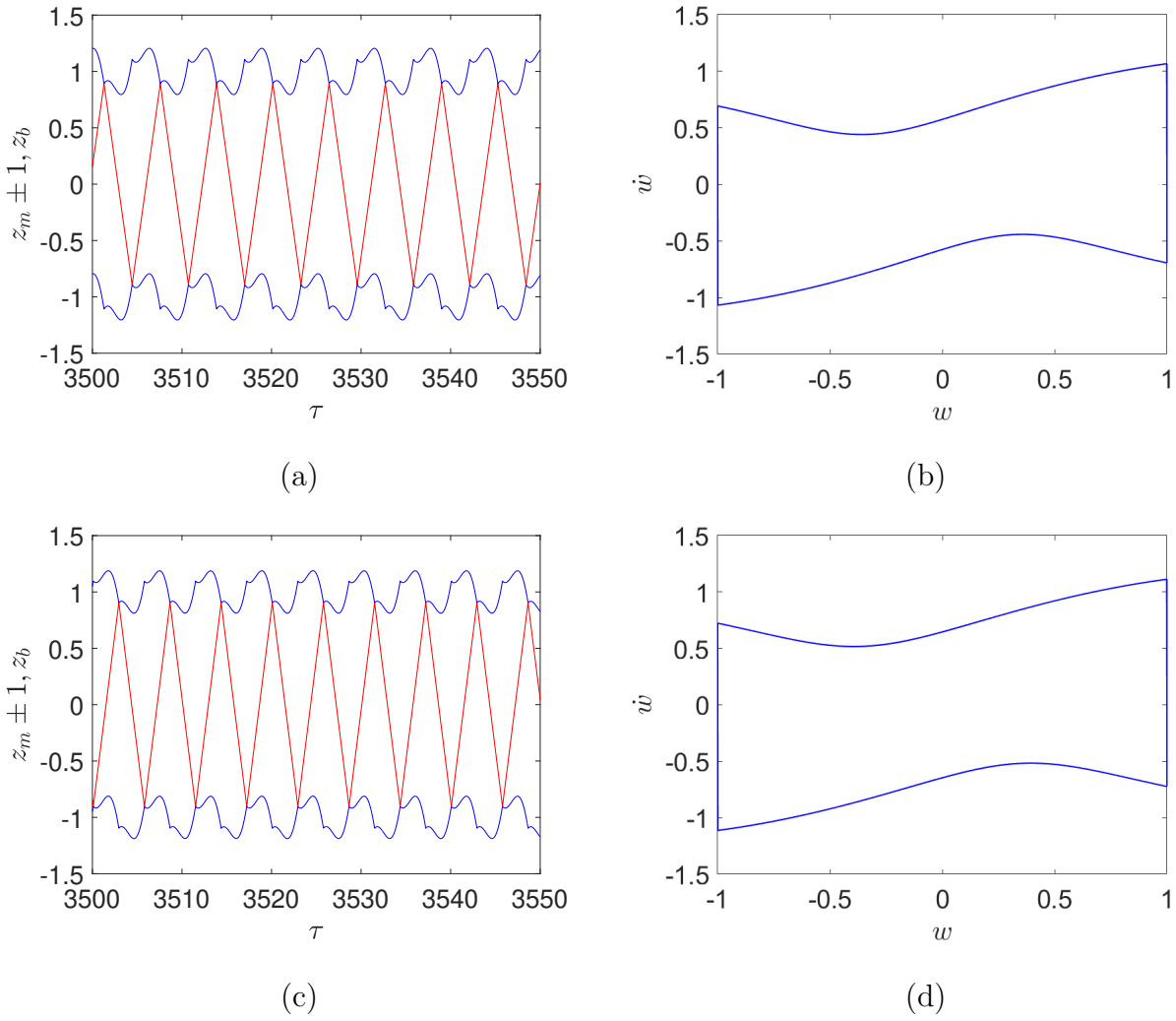

Figure 10: Time history (first column) of the non-dimensional displacement of the LO and the ball and the corresponding phase portrait (second column) of the system when the amplitude of excitation is $F = 0.4$. Parameters used for first row: $\Omega = 1, \eta = 0.55$; for second row: $\Omega = 1.1, \eta = 0.45$.

4.2. Dependence of 1:1 solution and alternating chatter on Ω

It should be noted that when the ball and the LO oscillate together with zero relative velocity (*e.g.* sticking motion), Eq. (5) becomes

$$(1+\eta)\ddot{z}_m + \eta\xi\dot{z}_m + z_m = F\sin(\Omega\tau+\varphi) + \eta\xi\Omega F\cos(\Omega\tau+\varphi). \tag{28}$$

Figure 11 compares the maximum displacement of the LO obtained by solving two different sets

of equations. The red line represents the solution obtained by solving Eqs. (5)-(6), while the black line depicts the solution of Eq. (28). Both panels illustrate how the alternating chatter phenomenon in Eqs. (5)-(6) results in a peak in the LO response near $\Omega \approx \omega_s/\omega_0 < 1$, while away from this value, where no chattering occurs, the response is different from that of Eq. (28). The peak response reflects that the repeated small velocity impacts of the alternating chatter, dominating the dynamics throughout the forcing period as shown in Fig. 9(c), effectively increase the mass of the system to $M+m$ for Ω near $\frac{\omega}{\omega_s}$. In both panels, the peaks for Eqs. (5)-(6) are smaller than the peak response of Eq. (28), since the alternating chatter only approximates a sticking-type behavior throughout a portion of the forcing period. In Fig. 11(a) the red peak response is slightly smaller

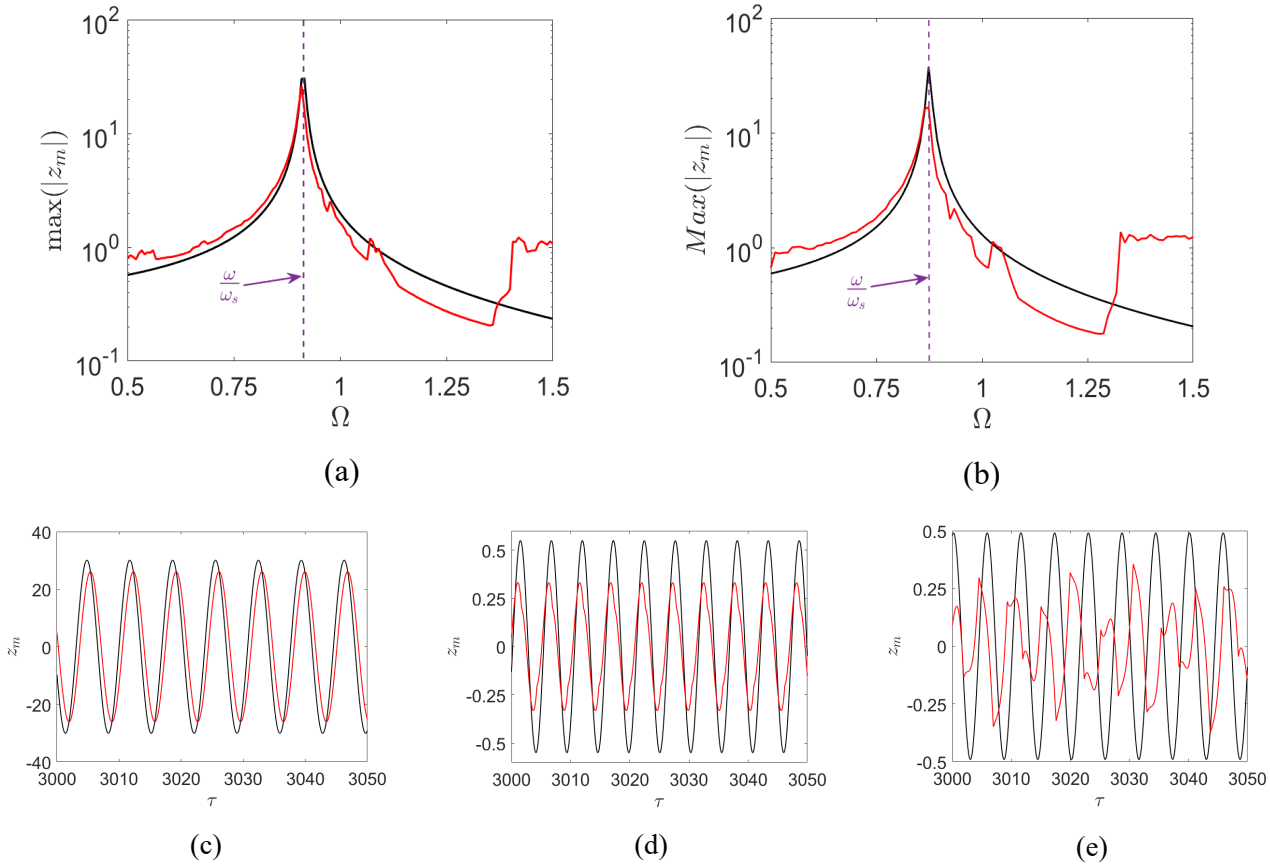

Figure 11: First row compares the maximum displacement of the LO for (a) $\eta = 0.2$ and (b) $\eta = 0.5$ by solving Eqs. (5)-(6) (red line) and Eq. (28) (black line) when $F = 0.4$. Note that the vertical axis is shown on a logarithmic scale. Second row shows the time histories to compare the dynamics obtained by solving Eq. (28) with that exhibited by VINES. Parameters are: (c) $\Omega = 0.909396$ ($\approx \frac{\omega}{\omega_s}$), $\eta = 0.2$, (d) $\Omega = 1.2, \eta = 0.2$, and (e) $\Omega = 1.1, \eta = 0.5$ when $F = 0.4$.

than the black peak response, indicating a stronger presence of alternating chatter in the system for $\eta = 0.2$.It can also be observed in Fig. 11(c) that the displacement time histories, obtained by solving Eqs. (5)-(6) and Eq. (28), are qualitatively similar for $\Omega \approx \frac{\omega}{\omega_s}$ and $\eta = 0.2$. On the other hand, for $\eta = 0.5$, the two peaks are shifted away from each other, indicating that the alternating chatter is less prominent as can be seen in the bifurcation diagram in Fig. 14(e). In the case of Eq. (28), energy dissipation occurs solely through damping, while in the case of Eqs. (5)-(6), energy is also dissipated through impacts, resulting in reduced amplitude. Figure 11 also emphasises the effect of η on ω_s by shifting the peak response away from $\Omega = 1$ with an increase in η. We note that this comparison is relevant only near the peak, i.e. near $\Omega = \frac{\omega}{\omega_s}$ as evident from Fig. 11(c). Away from this peak the comparison is not relevant, since the black curve is obtained by assuming that the ball and the LO are moving together as a single entity, while Eqs. (5)-(6) indicate that they do not move together for Ω away from $\frac{\omega}{\omega_s}$ as observed in Figs. 11(d) and (e).

Figure 12 provides insights into the influence of frequency ratio Ω and mass ratio η on the energy transfer measures for different forcing amplitude values. It is observed that as the input energy increases (from left to right) with increasing F, the parameter range over which a significant amount of energy is absorbed by the ball also expands. These findings confirm that with suitable combinations of parameters, remarkable vibration attenuation can be achieved in real engineering systems subjected to external excitation of $\mathcal{O}(1)$. Moreover, the figures indicate that higher forcing amplitude and/or mass ratio are not always suitable for effective TET. For instance, when $F = 0.2$ and $\eta = 0.5$; refer Fig. 13(c), there is no significant reduction in the maximum displacement of the LO and the KE ratio $\frac{K_b}{K_m+K_b}$ is relatively low compared to Figs. 13(a) and (b), which is not desirable for efficient TET. Therefore, for effective energy transfer, it is important to have larger forcing amplitude F for higher η, see Fig. 13(i) where $F = 0.4, \eta = 0.5$. However, Figs. 13(d) and (g) demonstrate that the opposite combination *i.e.*, a small η with a larger F for specific Ω, is also suitable for effective TET. Furthermore, Fig. 13 reveals that the maximum displacement does not necessarily occur near $\Omega = 1$. Due to the presence of the heavy ball, the maximum displacement shifts to the left (away from $\Omega = 1$) where ω_s aligns with the forcing frequency ω. However, for a specific η value, the system exhibits maximum response at the same Ω with increasing F as evident in each column of Fig. 13.

In addition to parameter combinations, the nature of the solution also significantly affects the effectiveness of energy transfer through VINES. To provide further insights into the performance of VINES, bifurcation diagrams are shown in Fig. 14, illustrating different periodic and chaotic regimes. These 3-D bifurcation diagrams are depicted for relative impact velocity as a function of the bifurcation parameters Ω and η for various values of F. In the first column of Fig. 14, focusing on $\Omega = 1$, it is observed that the window of 1:1 periodic solutions becomes wider and shifts towards the higher values of η as the amplitude of excitation increases. These 1:1 periodic windows, as shown in Fig. 12 for $\Omega = 1$, correspond to larger values of $\frac{K_b}{K_m+K_b}$ and lower maximum displacement of the LO in the $\eta - \Omega$ plane. Moreover, the occurrence of chattering behavior, as shown in Figs. 9(c) and (d), shifts towards lower η as the system approaches $\Omega = 1$ and the magnitude of relative impact

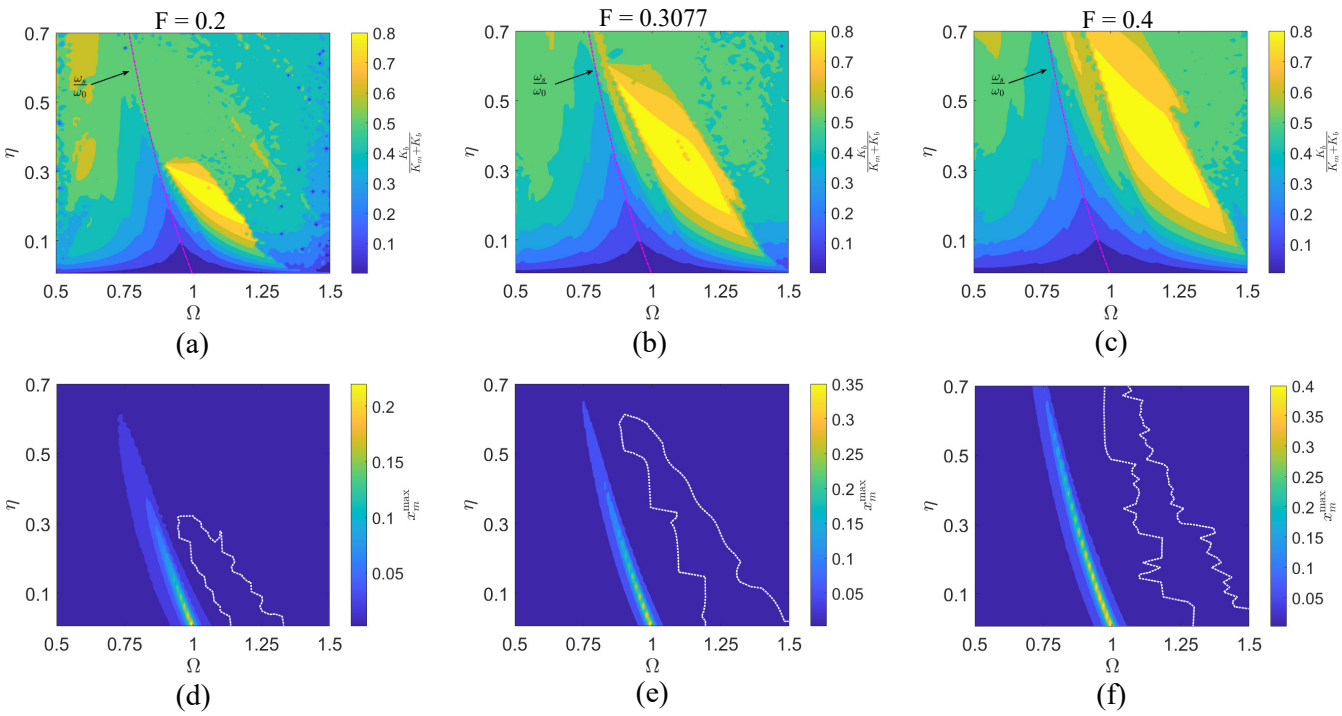

Figure 12: Effect of variation of mass ratio η and frequency ratio Ω on the maximum displacement of the LO and on the (KE) energy transfer to the ball. First column, (a) and (d), corresponds to $F = 0.2$; second column, (b) and (e), corresponds to $F = 0.3077$; last column, (c) and (f), corresponds to $F = 0.4$. The dashed pink line in (a)-(c) shows the effect of $\eta \equiv \mathcal{O}(1)$ on the variation of $\Omega \approx \frac{\omega_s}{\omega_0}$. The white region marked in (d)-(f) highlights the parameters range for which energy transfer is maximum and corresponds to the stable 1:1 periodic solution; see Fig. 16 for detail.

velocity increases for larger F. In these parametric combinations one can expect the displacement of the LO to increase while $\frac{K_b}{K_m+K_b}$ decreases as shown in Fig. 12. Moving to the second column of Fig. 14 (when $\Omega > 1$), it can be observed that the range of η for which the system exhibits 1:1 periodic behavior shifts towards lower values of η as Ω increases. Furthermore, the width of the 1:1 periodic solution window expands for increasing amplitude of excitation when $\Omega \geq 1$. Therefore, it can be concluded that the parametric combination of larger F with larger η yields a higher $\frac{K_b}{K_m+K_b}$ and a lower $x_m^{\max}$ for $\Omega \geq 1$, resulting in efficient energy transfer. Also, with increasing F, the boundaries of 1:1 solution appear to exhibit deterioration as seen in Fig. 12(f). Nonetheless, it is worth noting that the efficient TET can still be achieved in a significant region around this 1:1 periodic solution as shown in Fig. 12(c). Fig. 14 also highlights the region where the system exhibits chaotic behavior, indicating irregular impacts between the LO and the ball within a forcing period. These chaotic regimes are associated with a decrease in the efficiency of VINES in vibration control.

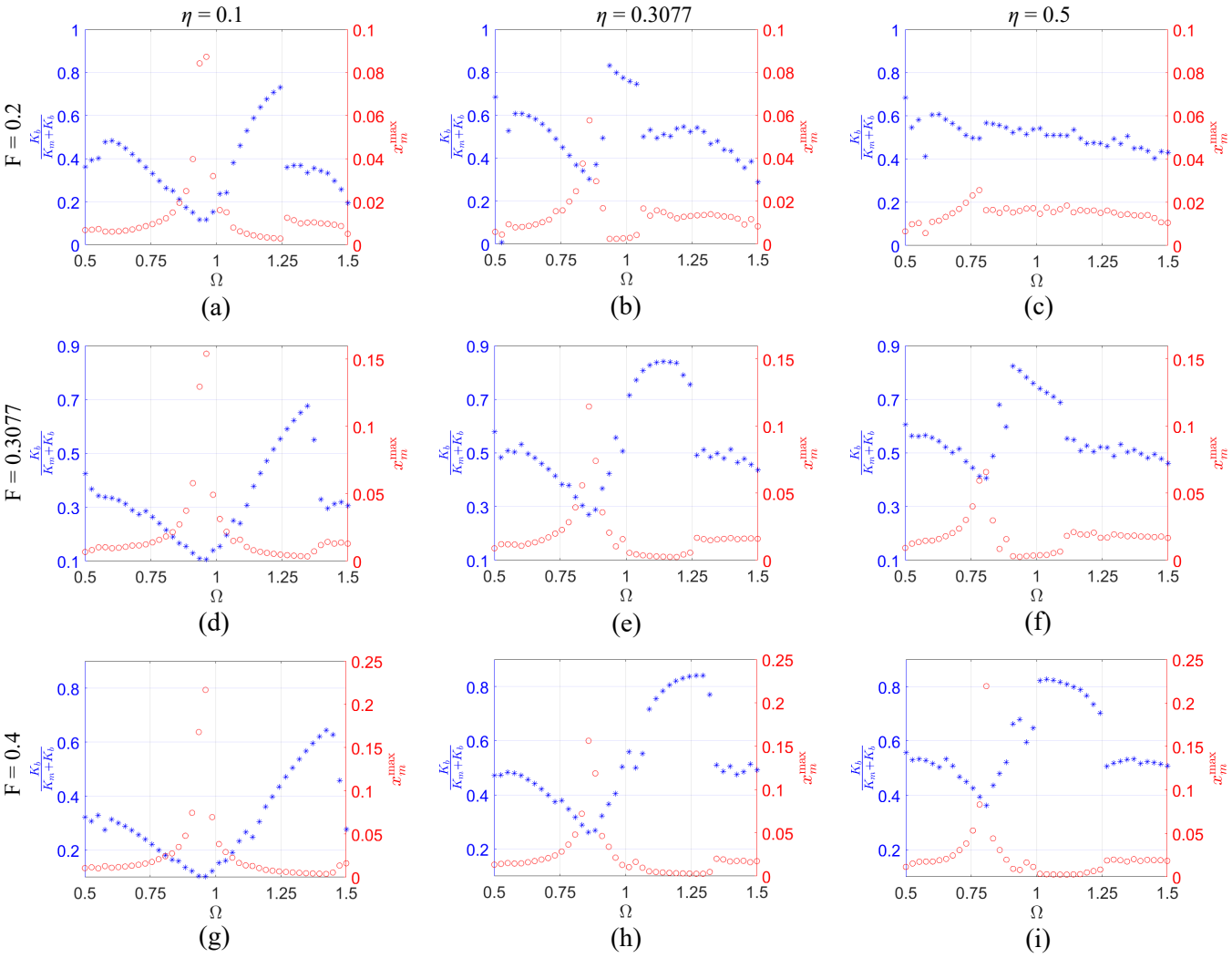

Figure 13: Sectional view of the contour plots shown in Fig. 12 for $F = 0.2, 0.3077$ and 0.4 (top to bottom) when $\eta = 0.1, 0.3077$ and 0.5 (left to right), respectively.

4.3. Complementary perspectives from the analysis

To ensure the stability of these periodic solutions, it is important to perform stability analysis. Figure 15(a) presents a comparison between the numerically obtained 1:1 periodic behavior for $\Omega = 0.9$ and the corresponding analytical solution. The similar comparison has been carried out for $\Omega = 1.1$ as shown in Fig. 15(c). Both cases ($\Omega > 1$ and $\Omega < 1$) exhibit very good agreement with each other, indicating the consistency of the results. The stability of these periodic solutions is examined by analyzing the magnitude of eigenvalues of $J_{P_2} J_{P_1}$ as a function of η. In Fig. 15(b) and (d), the variation of magnitude of eigenvalues are shown for $\Omega = 0.9$ and 1.1, respectively. Based

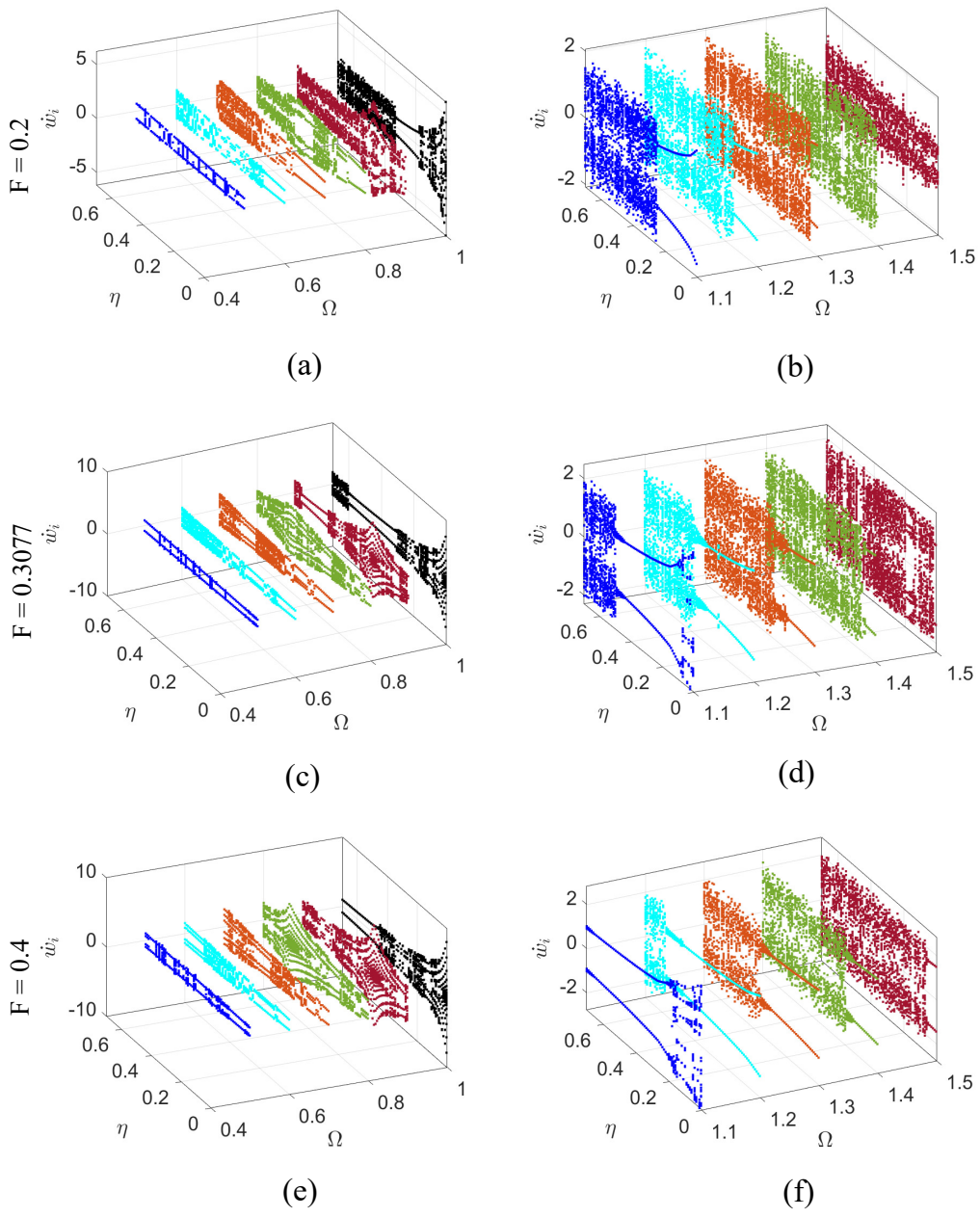

Figure 14: 3-D bifurcation diagrams of the relative impact velocity as the parameters η and Ω are varied. The amplitude of excitation (F) is 0.2 for (a), (b); 0.3077 for (c), (d) and 0.4 for (e), (f).

on the values of $|\lambda|$, stable (solid red line) and unstable (dotted red line) solutions are marked in Fig. 15(a) and (b). Notably, unlike in Fig. 6(b) and (d) where $\Omega = 1$, all eigenvalues in this case

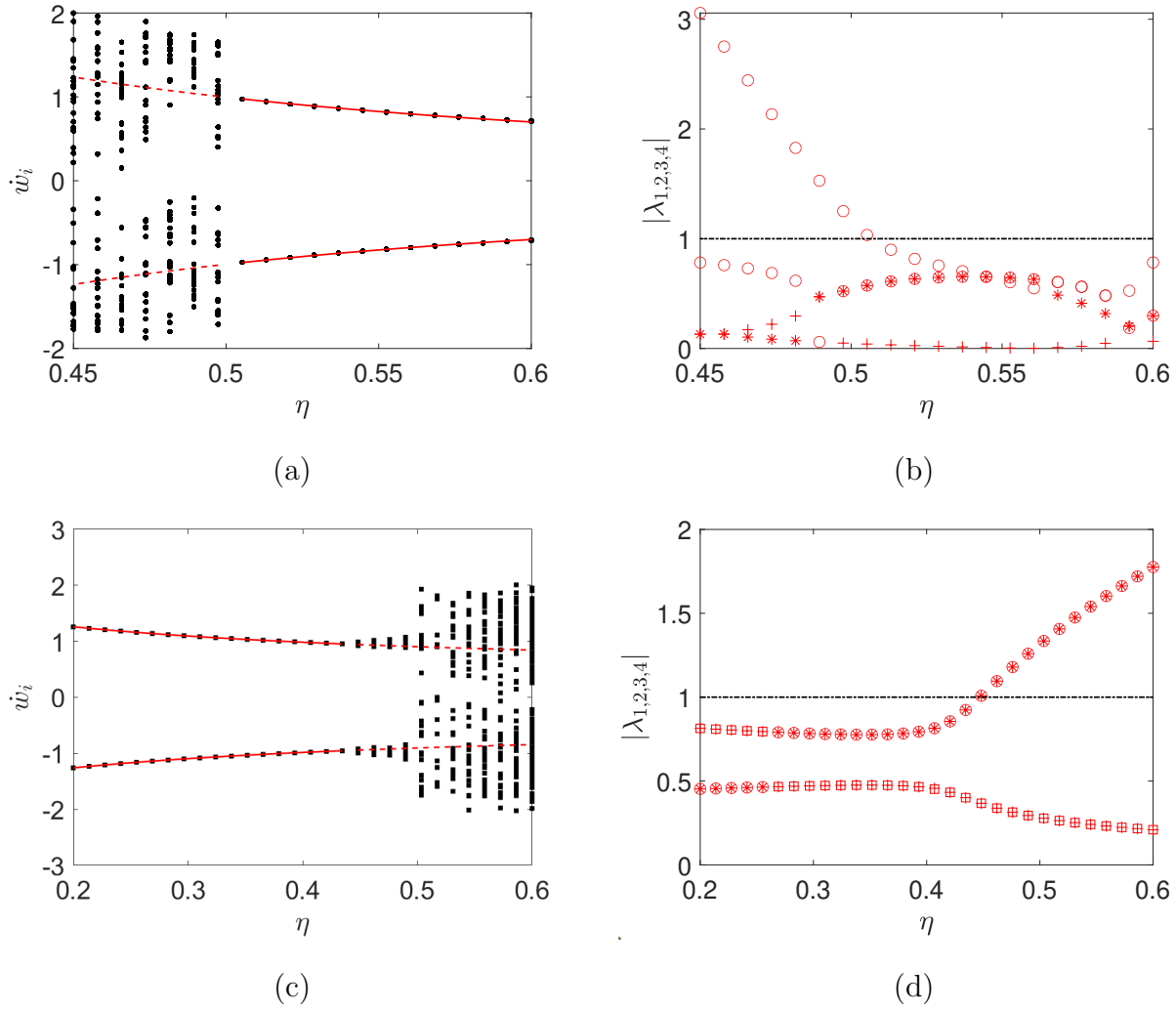

Figure 15: Zoomed view of the numerically obtained bifurcation diagrams (black dots) presented in Fig 14 which are supplemented with the analytically obtained 1:1 solution (red line) when (a) $F = 0.3077, \Omega = 0.9$ and (c) $F = 0.3077, \Omega = 1.1$. Solid line corresponds to stable solution whereas the broken line shows unstable solutions. For the stability of the solutions corresponding to these parameter sets, the magnitude of eigenvalues of the matrix $J_{P_2} J_{P_1}$ are shown in (b) and (d).

are significantly distant from the $|\lambda| = 1$ line for the stable solution, suggesting that the system is less susceptible to small parametric perturbations that could lead to instabilities.

The stability analysis of the 1:1 periodic solution is carried out in the $\eta - \Omega$ parameter space and the results are depicted in Fig. 16, showing the magnitude of the largest eigenvalue ($|\lambda_{\max}|$) of the matrix $J_{P_2} J_{P_1}$ for different forcing amplitudes. The orange color regions represent the symmetric

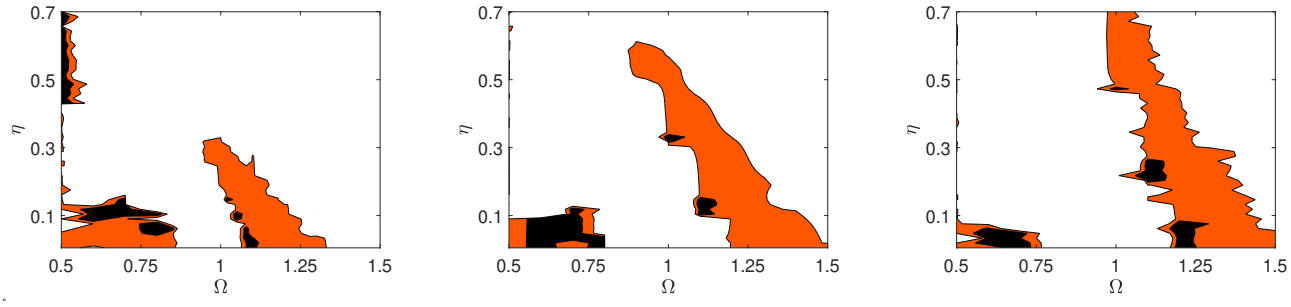

Figure 16: Based on the stability analysis for 1:1 solution,the magnitude of maximum eigenvalue ($|\lambda_{\max}|$) corresponding to different η and Ω is obtained for (a) $F = 0.2$, (b) $F = 0.3077$ and (c) $F = 0.4$. The orange and black regions have $|\lambda_{\max}|$ less than unity which corresponds to symmetric and asymmetric stable 1:1 periodic solution. The white regions have $|\lambda_{\max}| > 1$ which correspond to unstable 1:1 solution.

stable 1:1 solution, while the black regions indicate the stable asymmetric 1:1 periodic solution ($|\lambda_{\max}| < 1$). On the other hand, the white region corresponds to the unstable 1:1 solution ($|\lambda_{\max}| > 1$). Comparing Fig. 12 and Fig. 16, it is evident that the regions exhibiting maximum energy transfer align with the stable 1:1 periodic behavior of the system. In addition, comparing to Fig. 14 especially for small η and Ω, we note that the 1:1 solutions in these parameter ranges are not apparent from the contour plot Fig. 12. These solutions provide efficient TET for small η, but their KE ratio does not stand out in comparison with the KE ratios for larger η. Therefore, Fig. 16 provides an additional tool for identifying the parametric regimes that facilitate efficient energy transfer in the $\eta - \Omega$ plane.

5. Conclusions and future directions

This study investigates a forced vibro-impact nonlinear energy sink (VINES) system, where energy is transferred from the LO to the ball through impacts. The VINES system comprises a cavity within the LO, allowing the ball to move without friction and interact with the cavity walls, thereby enabling vibration control of the system. Unlike previous studies that focused on small parameter values and analysed the system near $\Omega = 1$, this study aims to explore the effectiveness of TET through VINES for larger parameter values, such as mass ratio and amplitude of excitation, over a broad frequency regime. To obtain analytical solutions for the two degrees-of-freedom VINES system, we employ a recently developed semi-analytical map based approach that utilizes the exact solutions. It is used to analytically obtain various periodic solutions and subsequently to discuss their stability. This approach provides flexibility in considering the various parametric combinations of interest and facilitates the analytical exploration for different periodic solutions and their stability

properties.

This manuscript presents a comprehensive investigation of energy transfer through VINES, ranging from small parameter values to a broad range of parameters. This study employs two measures to quantify the effectiveness of energy transfer: the ratio of the KE of the ball to the KE of the system and the maximum displacement of the LO. For practical engineering applications, the desired scenarios involve the ratio of KE to be high and sufficiently small $x_m^{\max}$ which can be achieved when the system exhibits 1:1 periodic behavior. Contour plots obtained through numerical simulations in the $\eta - \Omega$ plane and $\eta - F$ plane delineate the parameter regimes where energy transfer exceeds 70%, accompanied by very small $x_m^{\max}$. Bifurcation diagrams corresponding to these parameter regimes reveal the presence of stable 1:1 periodic behavior, while the chaotic dynamics are observed in the regions where energy transfer is less effective. The salient outcomes from this study can be summarized as follows:

- The study reveals that significant energy transfer can be achieved in broader parameter regimes away from $\Omega = 1$ by carefully selecting suitable combination of parameters, resulting in effective vibration attenuation with reduced $x_m^{\max}$. Furthermore, it is observed that parameter combination leading to out-of-phase, *i.e.*, impact phase $\varphi_i \in (\pi, 2\pi)$, impacts between the ball and the LO contribute to efficient energy transfer and decreased LO vibration amplitude.

- In contrast to previous studies that emphasize the maximum displacement occurring near $\Omega = 1$, this study demonstrates that the peak response can occur at different values of Ω. Specifically, it is observed that the peak displacement shifts to the left of $\Omega = 1$ as η increases. This finding provides valuable insights for the designer, as they can carefully select an appropriate η value to ensure smooth operation of the LO near the resonant condition. However, it is important to note that the location of the peak response remains unaltered for a specific η when the amplitude of excitation F is varied.

- This study reveals that a greater value of η and larger amplitude of excitation F do not necessarily guarantee efficient TET through VINES. The findings demonstrate that when F is smaller than η, the amplitude of vibration is relatively large compared to other cases and the KE energy ratio is also low, which is not favourable from the perspective of efficient energy transfer. However, for the opposite scenario where η is larger than F, the TET mechanism through VINES performs well. These results highlight the importance of considering the interplay between η and F in achieving efficient energy transfer.

- The linear stability analysis reveals interesting findings regarding the stability of the 1:1 periodic solutions. For $\Omega = 1$, the magnitude of eigenvalues of $J_{P_2} J_{P_1}$ associated with the stable solutions are slightly below unity, indicating a close proximity to the stability boundary. However, when $\Omega \neq 1$, the stable 1:1 solutions exhibit $0 < |\lambda_{1,2,3,4}| < 1$ and are sufficiently distant from the $|\lambda| = 1$ boundary. Then the 1:1 periodic solution for $\Omega \neq 1$ are robust against

small random fluctuations in excitation or parameter values. These stability characteristics contribute to the effectiveness and reliability of the TET mechanism in the VINES system.

A host of literature has extensively investigated the performance of VINES in energy transfer analytically, numerically as well as experimentally when parameters like η and F are small and $\Omega \approx 1$. This study takes a novel approach by numerically and analytically exploring the potential for effective TET through VINES across a broader range of parameters and Ω away from 1. The authors of this manuscript acknowledge that experimental validation of the findings is an important future work. In this regard, the experimental set-up at the Institute of Sound and Vibration Research, University of Southampton is underway, with the aim of conducting the experiments based on the insights and results reported in this study.

To enhance the realism of the mathematical model, the inclusion of friction is crucial. However, incorporating friction introduces additional complexities due to the discontinuity across $\dot{w} = 0$. A recent numerical study [23] has shown that friction can improve the performance of the system by expanding the window of 1:1 periodic solutions. However, the presence of friction also introduces sticking and sliding dynamics, necessitating further analysis to understand the performance of system in such scenarios. Additionally, to complement the numerical results, an analytical map-based framework utilizing exact solutions should be developed. Furthermore, the effect of noise on the performance of vibro-impact system in energy transfer needs to be investigated. The stability analysis has revealed a few cases where the magnitude of eigenvalues is close to 1. Therefore, investigating the behavior of such cases under the influence of noise would be an interesting avenue of research.

Acknowledgments

The authors are thankful to NSF, USA (Grant # CMMI/DMS 2009270) and EPSRC, UK (Grant # EP/V034391/1) for providing the financial support for the study reported in this paper.

Appendix A. Expressions for the Jacobian matrix

The entries of the Jacobian matrix mentioned in Eq. (27) can be obtained through implicit differentiation of Eqs. (12)-(15). Taking the derivative of Eq. 14 with respect to $\dot{z}_{m,i-1}, \dot{z}_{b,i-1}, z_{b,i-1}, \tau_{i-1}$

gives

$$\begin{aligned}
\frac{\partial z_{b,i}}{\partial \dot{z}_{m,i-1}} &= \mathcal{A}\frac{\partial \tau_i}{\partial \dot{z}_{m,i-1}} + \frac{1+r}{1+\eta}(\tau_i - \tau_{i-1}),\\
\frac{\partial z_{b,i}}{\partial \dot{z}_{b,i-1}} &= \mathcal{A}\frac{\partial \tau_i}{\partial \dot{z}_{b,i-1}} + \frac{\eta-r}{1+\eta}(\tau_i - \tau_{i-1}),\\
\frac{\partial z_{b,i}}{\partial z_{b,i-1}} &= \mathcal{A}\frac{\partial \tau_i}{\partial z_{b,i-1}} + 1,\\
\frac{\partial z_{b,i}}{\partial \tau_{i-1}} &= \mathcal{A}\left(\frac{\partial \tau_i}{\partial \tau_{i-1}} - 1\right),
\end{aligned} \tag{A.1}$$

where, $\mathcal{A} = \left(\frac{1+r}{1+\eta}\dot{z}_{m,i-1} + \frac{\eta-r}{1+\eta}\dot{z}_{b,i-1}\right)$. Next, using the relation $z_{b,i} = z_{m,i} \pm 1$, we can get

$$\begin{aligned}
\frac{\partial z_{b,i}}{\partial \dot{z}_{b,i-1}} = {} & \frac{\partial p_{1,i-1}}{\partial \dot{z}_{b,i-1}} e^{-\frac{\eta\xi\tau_i}{2}} \sin\alpha\tau_i + p_{1,i-1} e^{-\frac{\eta\xi\tau_i}{2}} \left(\frac{-\eta\xi}{2}\sin\alpha\tau_i + \alpha\cos\alpha\tau_i\right)\frac{\partial \tau_i}{\partial \dot{z}_{b,i-1}}\\
& + \frac{\partial p_{2,i-1}}{\partial \dot{z}_{b,i-1}} e^{-\frac{\eta\xi\tau_i}{2}} \cos\alpha\tau_i + p_{2,i-1} e^{-\frac{\eta\xi\tau_i}{2}} \left(\frac{-\eta\xi}{2}\cos\alpha\tau_i - \alpha\sin\alpha\tau_i\right)\frac{\partial \tau_i}{\partial \dot{z}_{b,i-1}}\\
& + \mathcal{B}\frac{\partial \tau_i}{\partial \dot{z}_{b,i-1}}.
\end{aligned} \tag{A.2}$$

Now, by comparing Eq. (A.2) with the second equation in Eq. (A.1), $\frac{\partial \tau_i}{\partial \dot{z}_{b,i-1}}$ can be written as

$$\frac{\partial \tau_i}{\partial \dot{z}_{b,i-1}} = \frac{\frac{\eta-r}{1+\eta}(\tau_i - \tau_{i-1}) - \frac{\partial p_{1,i-1}}{\partial \dot{z}_{b,i-1}} e^{-\frac{\eta\xi\tau_i}{2}} \sin\alpha\tau_i - \frac{\partial p_{2,i-1}}{\partial \dot{z}_{b,i-1}} e^{-\frac{\eta\xi\tau_i}{2}} \cos\alpha\tau_i}{\Delta}, \tag{A.3}$$

where, $\Delta = e^{-\frac{\eta\xi\tau_i}{2}} p_{1,i-1}\left(\frac{-\eta\xi}{2}\sin\alpha\tau_i + \alpha\cos\alpha\tau_i\right) + e^{-\frac{\eta\xi\tau_i}{2}} p_{2,i-1}\left(\frac{-\eta\xi}{2}\cos\alpha\tau_i - \alpha\sin\alpha\tau_i\right) + \mathcal{B} - \mathcal{A}$. Here, $\mathcal{B} = \Omega q_1 \cos(\Omega\tau_i + \varphi) - \Omega q_2 \sin(\Omega\tau_i + \varphi)$, $\frac{\partial p_{1,i-1}}{\partial \dot{z}_{b,i-1}} = e^{\frac{\eta\xi\tau_{i-1}}{2}} \cos(\alpha\tau_{i-1})\frac{\eta(1+r)}{\alpha(1+\eta)}$ and $\frac{\partial p_{2,i-1}}{\partial \dot{z}_{b,i-1}} = -e^{\frac{\eta\xi\tau_{i-1}}{2}} \sin(\alpha\tau_{i-1})\frac{\eta(1+r)}{\alpha(1+\eta)}$. Similarly, one can get the partial derivatives of τ_i with respect to the

other variables $(\dot{z}_{m,i-1}, z_{b,i-1}, \tau_{i-1})$ as

$$\frac{\partial \tau_i}{\partial \dot{z}_{m,i-1}} = \frac{\frac{1+r}{1+\eta}(\tau_i - \tau_{i-1}) - \frac{\partial p_{1,i-1}}{\partial \dot{z}_{m,i-1}} e^{-\frac{\eta\xi\tau_i}{2}} \sin\alpha\tau_i - \frac{\partial p_{2,i-1}}{\partial \dot{z}_{m,i-1}} e^{-\frac{\eta\xi\tau_i}{2}} \cos\alpha\tau_i}{\Delta}, \tag{A.4}$$

$$\frac{\partial \tau_i}{\partial z_{b,i-1}} = \frac{1 - \frac{\partial p_{1,i-1}}{\partial z_{b,i-1}} e^{-\frac{\eta\xi\tau_i}{2}} \sin\alpha\tau_i - \frac{\partial p_{2,i-1}}{\partial z_{b,i-1}} e^{-\frac{\eta\xi\tau_i}{2}} \cos\alpha\tau_i}{\Delta}, \tag{A.5}$$

$$\frac{\partial \tau_i}{\partial \tau_{i-1}} = \frac{-\mathcal{A} - \frac{\partial p_{1,i-1}}{\partial \tau_{i-1}} e^{-\frac{\eta\xi\tau_i}{2}} \sin\alpha\tau_i - \frac{\partial p_{2,i-1}}{\partial \tau_{i-1}} e^{-\frac{\eta\xi\tau_i}{2}} \cos\alpha\tau_i}{\Delta}. \tag{A.6}$$

Here,

$$\frac{\partial p_{1,i-1}}{\partial \dot{z}_{m,i-1}} = e^{\frac{\eta\xi\tau_{i-1}}{2}} \cos(\alpha\tau_{i-1}) \frac{(1-\eta r)}{\alpha(1+\eta)} \text{ and } \frac{\partial p_{2,i-1}}{\partial \dot{z}_{m,i-1}} = -e^{\frac{\eta\xi\tau_{i-1}}{2}} \sin(\alpha\tau_{i-1}) \frac{(1-\eta r)}{\alpha(1+\eta)}, \tag{A.7}$$

$$\begin{aligned} \frac{\partial p_{1,i-1}}{\partial z_{b,i-1}} &= -e^{\frac{\eta\xi\tau_{i-1}}{2}} \left(\frac{-\eta\xi}{2\alpha} \cos(\alpha\tau_{i-1}) - \sin(\alpha\tau_{i-1}) \right), \\ \frac{\partial p_{2,i-1}}{\partial z_{b,i-1}} &= -e^{\frac{\eta\xi\tau_{i-1}}{2}} \left(\frac{\eta\xi}{2\alpha} \sin(\alpha\tau_{i-1}) - \cos(\alpha\tau_{i-1}) \right), \end{aligned} \tag{A.8}$$

$$\begin{aligned} \frac{\partial p_{1,i-1}}{\partial \tau_{i-1}} &= \frac{\eta\xi}{2} p_{1,i-1} - \frac{e^{\frac{\eta\xi\tau_{i-1}}{2}}}{\alpha} \left[\left(\frac{\eta\xi\alpha}{2} \sin(\alpha\tau_{i-1}) - \alpha^2 \cos(\alpha\tau_{i-1}) \right) (z_{m,i-1} - \mathcal{C}) \right] \\ &\quad - \mathcal{B} \left(-\frac{\eta\xi}{2} \cos(\alpha\tau i - 1) - \alpha \sin(\alpha\tau_{i-1}) \right) - \Omega^2 \mathcal{C} \cos(\alpha\tau_{i-1}) \\ &\quad + \alpha \sin(\alpha\tau_{i-1}) \left(\frac{1-\eta r}{1+\eta} \dot{z}_{m,i-1} + \frac{\eta(1+r)}{1+\eta} \dot{z}_{b,i-1} - \mathcal{B} \right), \\ \frac{\partial p_{2,i-1}}{\partial \tau_{i-1}} &= -\frac{\eta\xi}{2} p_{2,i-1} - \frac{e^{\frac{\eta\xi\tau_{i-1}}{2}}}{\alpha} \left[\left(\frac{\eta\xi\alpha}{2} \cos(\alpha\tau_{i-1}) - \alpha^2 \sin(\alpha\tau_{i-1}) \right) (z_{m,i-1} - \mathcal{C}) \right] \\ &\quad - \mathcal{B} \left(\frac{\eta\xi}{2} \sin(\alpha\tau i - 1) - \alpha \cos(\alpha\tau_{i-1}) \right) + \Omega^2 \mathcal{C} \sin(\alpha\tau_{i-1}) \\ &\quad + \alpha \cos(\alpha\tau_{i-1}) \left(\frac{1-\eta r}{1+\eta} \dot{z}_{m,i-1} + \frac{\eta(1+r)}{1+\eta} \dot{z}_{b,i-1} - \mathcal{B} \right), \end{aligned} \tag{A.9}$$

where, $\mathcal{C} = q_1 \sin(\Omega\tau_{i-1} + \varphi) + q_2 \cos(\Omega\tau_{i-1} + \varphi)$. Finally, taking the derivative of $\dot{z}_{m,i}$ with respect to $(\dot{z}_{m,i-1}, \dot{z}_{b,i-1}, z_{b,i-1}, \tau_{i-1})$, respectively, gives

$$\begin{aligned}
\frac{\partial \dot{z}_{m,i}}{\partial \dot{z}_{m,i-1}} &= e^{-\frac{\eta\xi\tau_i}{2}} \left(\frac{-\eta\xi}{2} \sin(\alpha\tau_i) + \alpha \cos(\alpha\tau_i) \right) \frac{\partial p_{1,i-1}}{\partial \dot{z}_{m,i-1}} - \Omega^2 \mathcal{C} \frac{\partial \tau_i}{\partial \dot{z}_{m,i-1}} \\
&+ e^{-\frac{\eta\xi\tau_i}{2}} p_{1,i-1} \left[\left(\frac{\eta^2\xi^2}{4} - r^2 \right) \sin(\alpha\tau_i) - \eta\xi\alpha \cos(\alpha\tau_i) \right] \frac{\partial \tau_i}{\partial \dot{z}_{m,i-1}} \\
&+ e^{-\frac{\eta\xi\tau_i}{2}} p_{2,i-1} \left[\left(\frac{\eta^2\xi^2}{4} - r^2 \right) \cos(\alpha\tau_i) + \eta\xi\alpha \sin(\alpha\tau_i) \right] \frac{\partial \tau_i}{\partial \dot{z}_{m,i-1}} \\
&+ e^{-\frac{\eta\xi\tau_i}{2}} \left(\frac{-\eta\xi}{2} \cos(\alpha\tau_i) - \alpha \sin(\alpha\tau_i) \right) \frac{\partial p_{2,i-1}}{\partial \dot{z}_{m,i-1}},
\end{aligned} \tag{A.10}$$

$$\begin{aligned}
\frac{\partial \dot{z}_{m,i}}{\partial \dot{z}_{b,i-1}} &= e^{-\frac{\eta\xi\tau_i}{2}} \left(\frac{-\eta\xi}{2} \sin(\alpha\tau_i) + \alpha \cos(\alpha\tau_i) \right) \frac{\partial p_{1,i-1}}{\partial \dot{z}_{b,i-1}} - \Omega^2 \mathcal{C} \frac{\partial \tau_i}{\partial \dot{z}_{b,i-1}} \\
&+ e^{-\frac{\eta\xi\tau_i}{2}} p_{1,i-1} \left[\left(\frac{\eta^2\xi^2}{4} - r^2 \right) \sin(\alpha\tau_i) - \eta\xi\alpha \cos(\alpha\tau_i) \right] \frac{\partial \tau_i}{\partial \dot{z}_{b,i-1}} \\
&+ e^{-\frac{\eta\xi\tau_i}{2}} p_{2,i-1} \left[\left(\frac{\eta^2\xi^2}{4} - r^2 \right) \cos(\alpha\tau_i) + \eta\xi\alpha \sin(\alpha\tau_i) \right] \frac{\partial \tau_i}{\partial \dot{z}_{b,i-1}} \\
&+ e^{-\frac{\eta\xi\tau_i}{2}} \left(\frac{-\eta\xi}{2} \cos(\alpha\tau_i) - \alpha \sin(\alpha\tau_i) \right) \frac{\partial p_{2,i-1}}{\partial \dot{z}_{b,i-1}},
\end{aligned} \tag{A.11}$$

$$\begin{aligned}
\frac{\partial \dot{z}_{m,i}}{\partial z_{b,i-1}} &= e^{-\frac{\eta\xi\tau_i}{2}} \left(\frac{-\eta\xi}{2} \sin(\alpha\tau_i) + \alpha \cos(\alpha\tau_i) \right) \frac{\partial p_{1,i-1}}{\partial z_{b,i-1}} - \Omega^2 \mathcal{C} \frac{\partial \tau_i}{\partial z_{b,i-1}} \\
&+ e^{-\frac{\eta\xi\tau_i}{2}} p_{1,i-1} \left[\left(\frac{\eta^2\xi^2}{4} - r^2 \right) \sin(\alpha\tau_i) - \eta\xi\alpha \cos(\alpha\tau_i) \right] \frac{\partial \tau_i}{\partial z_{b,i-1}} \\
&+ e^{-\frac{\eta\xi\tau_i}{2}} p_{2,i-1} \left[\left(\frac{\eta^2\xi^2}{4} - r^2 \right) \cos(\alpha\tau_i) + \eta\xi\alpha \sin(\alpha\tau_i) \right] \frac{\partial \tau_i}{\partial z_{b,i-1}} \\
&+ e^{-\frac{\eta\xi\tau_i}{2}} \left(\frac{-\eta\xi}{2} \cos(\alpha\tau_i) - \alpha \sin(\alpha\tau_i) \right) \frac{\partial p_{2,i-1}}{\partial z_{b,i-1}},
\end{aligned} \tag{A.12}$$

$$
\begin{aligned}
\frac{\partial \dot{z}_{m,i}}{\partial \tau_{i-1}} = & e^{-\frac{\eta\xi\tau_i}{2}} \left(\frac{-\eta\xi}{2} \sin(\alpha\tau_i) + \alpha \cos(\alpha\tau_i) \right) \frac{\partial p_{1,i-1}}{\partial \tau_{i-1}} - \Omega^2 \mathcal{C} \frac{\partial \tau_i}{\partial \tau_{i-1}} \\
& + e^{-\frac{\eta\xi\tau_i}{2}} p_{1,i-1} \left[\left(\frac{\eta^2\xi^2}{4} - r^2 \right) \sin(\alpha\tau_i) - \eta\xi\alpha \cos(\alpha\tau_i) \right] \frac{\partial \tau_i}{\partial \tau_{i-1}} \\
& + e^{-\frac{\eta\xi\tau_i}{2}} p_{2,i-1} \left[\left(\frac{\eta^2\xi^2}{4} - r^2 \right) \cos(\alpha\tau_i) + \eta\xi\alpha \sin(\alpha\tau_i) \right] \frac{\partial \tau_i}{\partial \tau_{i-1}} \\
& + e^{-\frac{\eta\xi\tau_i}{2}} \left(\frac{-\eta\xi}{2} \cos(\alpha\tau_i) - \alpha \sin(\alpha\tau_i) \right) \frac{\partial p_{2,i-1}}{\partial \tau_{i-1}}.
\end{aligned}
\tag{A.13}
$$

References

[1] L. Serdukova, R. Kuske, D. Yurchenko, Stability and bifurcation analysis of the period-t motion of a vibroimpact energy harvester, Nonlinear Dynamics 98 (2019) 1807–1819.

[2] H. Li, A. Li, Potential of a vibro-impact nonlinear energy sink for energy harvesting, Mechanical Systems and Signal Processing 159 (2021) 107827.

[3] L. Serdukova, R. Kuske, D. Yurchenko, Post-grazing dynamics of a vibro-impacting energy generator, Journal of Sound and Vibration 492 (3) (2021) 115811.

[4] A. F. Vakakis, O. V. Gendelman, L. A. Bergman, A. Mojahed, M. Gzal, Nonlinear targeted energy transfer: state of the art and new perspectives, Nonlinear Dynamics 108 (2022) 711–741.

[5] Z. Chen, H. Fang, Z. Han, S. Sun, Influence of bridge-based designed tmd on running trains, Journal of Vibration and Control 25 (1) (2019) 182–193.

[6] O. V. Gendelman, Y. Starosvetsky, M. Feldman, Attractors of harmonically forced linear oscillator with attached nonlinear energy sink i: Description of response regimes, Nonlinear Dynamics 51 (2008) 31–46.

[7] H. Li, A. Li, X. Kong, H. Xiong, Dynamics of an electromagnetic vibro-impact nonlinear energy sink, applications in energy harvesting and vibration absorption, Nonlinear Dynamics 108 (2022) 1807–1819.

[8] D. Hong, T. L. Hill, S. A. Neild, Understanding targeted energy transfer from a symmetry breaking perspective, Proceedings of the Royal Society A 477 (2021) 20210045.

[9] P. Kumar, S. Narayanan, S. Gupta, Targeted energy transfer in stochastically excited system with nonlinear energy sink, European Journal of Applied Mathematics 30 (2019) 369–886.

[10] H. Yao, Y. Cao, S. Zhang, B. Wen, A novel energy sink with piecewise linear stiffness, Nonlinear Dynamics 94 (2018) 2265–2275.

[11] X. Kong, H. Li, C. Wu, Dynamics of 1-dof and 2-dof energy sink with geometrically nonlinear damping: application to vibration suppression, Nonlinear Dynamics 91 (2018) 733–754.

[12] O. V. Gendelman, Analytic treatment of a system with a vibro-impact nonlinear energy sink, Journal of Sound and Vibration 331 (2012) 4599–4608.

[13] O. Gendelman, A. Alloni, Dynamics of forced system with vibro-impact energy sink, Journal of Sound and Vibration 358 (2015) 301–314.

[14] Y. S. Lee, F. Nucera, A. F. Vakakis, D. M. McFarland, L. A. Bergman, Periodic orbits, damped transitions and targeted energy transfers in oscillators with vibro-impact attachments, Physica D: Nonlinear Phenomena 238 (2009) 1868–1896.

[15] A. C. J. Luo, Y. Guo, Vibro-Impact Dynamics, John Wiley & Sons Ltd, Oxford, UK, 2013.

[16] W. Li, N. E. Wierschem, X. Li, T. Yang, On the energy transfer mechanism of the single-sided vibro-impact nonlinear energy sink, Journal of Sound and Vibration 437 (2018) 166–179.

[17] Y. M. Wei, X. J. Dong, P. F. Guo, Z. K. Peng, W. M. Zhang, Enhanced targeted energy transfer by vibro impact cubic nonlinear energy sink, International Journal of Applied Mechanics 10 (2018) 1850061.

[18] Z. Wu, M. Paredes, S. Seguy, Targeted energy transfer in a vibro-impact cubic nes: Description of regimes and optimal design, Journal of Sound and Vibration 545 (2023) 117425.

[19] T. Li, S. Seguy, A. Berlioz, Dynamics of cubic and vibro-impact nonlinear energy sink: Analytical, numerical, and experimental analysis, Journal of Vibration and Acoustics 138 (2016) 031010.

[20] B. Youssef, R. I. Leine, A complete set of design rules for a vibro-impact nes based on a multiple scales approximation of a nonlinear mode, Journal of Sound and Vibration 501 (2021) 116043.

[21] T. Li, S. Seguy, A. Berlioz, Optimization mechanism of targeted energy transfer with vibro-impact energy sink under periodic and transient excitation, Nonlinear Dynamics 87 (2016) 2415–2433.

[22] T. Li, C.-H. Lamarque, S. Seguy, A. Berlioz, Chaotic characteristic of a linear oscillator coupled with vibro-impact nonlinear energy sink, Nonlinear Dynamics 91 (2018) 2319–2330.

[23] H. Li, A. Li, Y. Zhang, Importance of gravity and friction on the targeted energy transfer of vibro-impact nonlinear energy sink, International Journal of Impact Engineering 157 (2021) 104001.

[24] T. Li, E. Gourc, S. Seguy, A. Berlioz, Dynamics of two vibro-impact nonlinear energy sinks in parallel under periodic and transient excitations, International Journal of Non-Linear Mechanics 90 (2017) 100–110.

[25] Y. Wei, S. Wei, Q. Zhang, X. Dong, Z. Peng, W. Zhang, Targeted energy transfer of a parallel nonlinear energy sink, Applied Mathematics and Mechanics 40 (2019) 621–630.

[26] R. Liu, R. Kuske, D. Yurchenko, Maps unlock the full dynamics of targeted energy transfer via a vibro-impact nonlinear energy sink, Mechanical Systems and Signal Processing 191 (2023) 110158.

[27] F. Nucera, A. F. Vakakis, D. M. McFarland, L. A. Bergman, G. Kerschen, Targeted energy transfers in vibro-impact oscillators for seismic mitigation, Nonlinear Dynamics 53 (2007) 651–677.

[28] T. Huang, D. M. McFarland, A. F. Vakakis, O. V. Gendelman, L. A. Bergman, H. Lu, Energy transmission by impact in a system of two discrete oscillators, Nonlinear Dynamics 100 (2020) 135–145.

[29] M. Gzal, A. F. Vakakis, L. A. Bergman, O. V. Gendelman, Extreme intermodal energy transfers through vibro-impacts for highly effective and rapid blast mitigation, Communications in Nonlinear Science and Numerical Simulation 103 (2021) 106012.

[30] E. Gourc, G. Michon, S. Seguy, A. Berlioz, Experimental investigation and design optimization of targeted energy transfer under periodic forcing, Journal of Vibration and Acoustics 136 (2014) 021021.

[31] E. Gourc, G. Michon, S. Seguy, A. Berlioz, Targeted energy transfer under harmonic forcing with a vibro-impact nonlinear energy sink: analytical and experimental developments, Journal of Vibration and Acoustics 137 (2015) 031008.

[32] M. di Bernardo, C. J. Budd, A. R. Champneys, P. Kowalczyk, Piecewise-smooth Dynamical Systems: Theory and Applications, Springer Verlag, London, 2008.

[33] R. I. Leine, H. Nijmeijer, Dynamics and Bifurcations of Non-Smooth Mechanical Systems, Springer Verlag, Berlin, 2004.

[34] R. Chawla, A. Rounak, V. Pakrashi, Stability analysis of hybrid systems with higher order transverse discontinuity mapping, arXiv (2022) 203.13222.